CYCLICAL REGULATION OF A CONTRACTILE TUBE:
INSIGHTS FROM THE *CAENORHABDITIS ELEGANS* SPERMATHECA
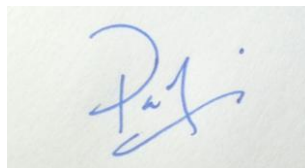
TAN PEI YI
(B. Sci. (Hons.), NUS)

A THESIS SUBMITTED
FOR THE DEGREE OF DOCTOR OF PHILOSOPHY
MECHANOBIOLOGY INSTITUTE
NATIONAL UNIVERSITY OF SINGAPORE

2015

DECLARATION

I hereby declare that this thesis is my original work and it has been written by me in its entirety. I have duly acknowledged all the sources of information which have been used in this thesis.

This thesis has also not been submitted for any degree in any university previously.

_____

Tan Pei Yi

13 August 2015

Acknowledgements

First of all, I would like to express my deepest gratitude to Dr Ronen Zaidel-Bar for giving me the opportunity to carry out my PhD studies under his supervision. He has been an excellent mentor who has displayed great patience and foresight, and his invaluable guidance and insightful suggestions has helped me immensely during the course of my work.

I would also like to thank my collaborators: Dr Nils Gauthier and Dr Toh Kee Chua for the work on mammalian PARG1, and Dr Erin Cram, Jeffery Bouffard and Alyssa Danielle for reagents and the work on calcium signalling in the spermatheca.

I am grateful to the members of my Thesis Advisory Committee: Dr Takao Inoue and Dr Yusuke Toyama for providing suggestions and guidance in my research throughout the years.

My sincere thanks go to my present and former lab mates: Megha, Wei Yung, Wu Yao, Anup, Gary, Zac, Jason, Yemima, Thang, Fen Yee, Cristina and Aish. I would like to express my gratefulness to them for always sharing their thoughts and giving me countless suggestions during my PhD studies and to some of them for being such great lunchtime buddies!

I would also like to thank Ida Sudol for being a wonderful student during her summer internship in the lab. She has contributed immensely to the preliminary characterization of RHGF-1 function in the spermatheca.

My appreciation goes to the Mechanobiology Institute, Singapore for awarding me with a PhD scholarship and the MBI Core Facilities personnel for providing a safe and conducive environment for me to carry out my research.

Finally, and most importantly, my profound gratitude goes to my family and my fiancé for their love and all the help they have provided me throughout the course of my work. Without their constant support, motivation and love, I would not have been able to finish this work.

Table of Contents

<u>Summary</u>

Actomyosin contractility in epithelial cells is a major force driving changes in tissue shape. Biochemical signaling pathways downstream of RhoA control actin assembly in conjunction with non-muscle myosin II recruitment and phosphorylation, thus playing an important role in regulating actomyosin contractility. In recent years evidence for the critical role physical forces play in regulating vital aspects of cell behavior, from differentiation to apoptosis, has been piling. External mechanical forces have been shown to impact RhoA activity and cellular contractility. Yet, a large gap remains in our understanding of how cells translate physical forces into biochemical signals to promote mechanoresponses.

During *C. elegans* ovulation, a single oocyte is propelled into a myoepithelial pouch termed the spermatheca. Upon fertilization of the oocyte, actomyosin contractility drives spermathecal constriction and facilitates the exit of the newly fertilized embryo into the uterus. During each ovulation cycle, entry of the oocyte into the spermatheca mechanically stretches the spermathecal cells. In this study, we utilize the intrinsic ability the *C. elegans* reproductive system to induce mechanical force in a cyclical manner to investigate RhoA activation downstream of mechanical stimuli in an in vivo setting.

Using a reverse genetics RNAi screen, we identified SPV-1 (a RhoGAP protein) and RHGF-1 (a RhoGEF protein) to be essential for the precise regulation of spermathecal contractility. SPV-1 functions to transduce physical cues from the membrane into a biochemical signal controlling contractility by transiently localizing to the apical

membrane of the spermatheca. SPV-1 localizes through its F-BAR domain to the membrane of the relaxed spermatheca, where it inhibits RHO-1/RhoA activity through its RhoGAP domain. Oocyte entry forces the spermatheca cells to stretch and as a consequence SPV-1 detaches from the membrane. RHGF-1 plays the opposite role by activating RHO-1 through its RhoGEF domain. The increase in RHO-1 activity facilitates spermatheca contraction and expulsion of the newly fertilized embryo into the uterus. This leads to re-formation of membrane folds in the collapsed spermatheca, SPV-1 reattachment to the membrane, and initiation of a new cycle.

Our results demonstrate how membrane curvature-dependent localization of an F-BAR domain coupled to a RhoGAP domain and the antagonistic function between a RhoGAP and RhoGEF protein can provide feedback between a mechanical signal and actomyosin contractility. We anticipate this to be a widely utilized feedback mechanism to balance actomyosin forces based on membrane topology both in the face of externally applied forces, as well as in situations when cells apply intrinsic forces, such as cell migration.

List of Tables

List of Figures

List of Abbreviations

ARHGAP 29/PARG1   Rho GTPase-activating protein 29

BAR   BIN/Amphiphysin/RVS

BAR-PH   BAR-pleckstrin homology

C1   Phorbolesters/diacylglycerol binding

CC   Coiled-coil

CCD   Charged-coupled device

CGC   *Caenorhabditis* Genetics Centre

DELTA-BLAST   Domain Enhanced Lookup Time Accelerated Basic Local Alignment Search Tool

DIC   Differential interference contrast

EMCCD   Evolve Rapid-Cal electron multiplying charged-coupled device

EpH4   Mouse mammary epithelial cell

F-BAR   Fes/CIP-4 homology-BAR

FRET   Förster resonance energy transfer

GMIP   GEM interacting protein

HMHA1   Human minor histocompatibility antigen 1

I-BAR   Inverse-BAR

IP3   Inositol 1,4,5-triphosphate

IPTG   Isopropyl β-D-1-thiogalactopyranoside

MEF   Mouse embryonic fibroblast

MLC   Myosin II regulatory light chain

MLCP   Myosin light chain phosphatase

MSP	Major sperm protein
N-BAR	N-terminal amphiphathic helix-BAR
NGM	Nematode growth medium
PDMS	Polydimethylsiloxane
PH	Plekstrin homology
PLCδ1	Phospholipase C gamma 1
PX-BAR	PhoX-BAR
RHGF-1	Rho guanine nucleotide exchange factor
RhoGAP	RhoGTPase activating protein
RhoGDI	RhoGTPase guanine nucleotide dissociation inhibitor
RhoGEF	RhoGTPase guanine nucleotide exchange factor
RNAi	RNA interference
ROCK	Rho kinase
RPTPα	Receptor-like tyrosine phosphatase α
sp-ut valve	Spermatheca-uterine valve
SPV-1	Spermatheca physiology varient 1
TEM	Transmission electron microscopy

Chapter 1:

Introduction

1. <u>Introduction</u>

Actomyosin contractility is a universal mechanism to organize cell shape changes in a plethora of cellular processes from cell migration and cytokinesis to morphogenic events in organisms (as reviewed in Zaidel-Bar et al. (2015)). Local activation of the small GTPase RhoA plays a major role in regulating contractility through promoting actin polymerization by diaphanous formins (Watanabe et al., 1999) and phosphorylation of myosin II regulatory light chain (MLC) by the serine/threonine Rho kinase (ROCK) (Amano et al., 1996). In the smooth muscle cells of epithelial tubes such as blood vessels and the airway, misregulation of the constriction events is the hallmark of various pathological diseases such as vascular hypertension and asthma (Chiba and Misawa, 2004; Loirand and Pacaud, 2010).

Cells are capable of sensing physical cues such as shear stress, tension, substrate stiffness and changes in cell geometry and respond through co-arrangements of actin and myosin to facilitate cell shape change. In some cases, mechanical forces arising internally or from external perturbations have been shown modulate contractility by regulating the activity of RhoA (as reviewed in Lessey et al. (2012)). The mechanism behind the 'mechanosensing' ability of cells has been an area of active research in the past decade. Although the signaling pathways downstream of RhoA are well characterized (Fukata et al., 2001; Van Eyk et al., 1998), the biomechanical regulation of RhoA activation is less well understood.

In this study, we aim to elucidate the mechanosensory pathways linking exogenous force to RhoA regulation. Much of the current understanding on how mechanical stimuli lead to RhoA activation is derived from in vitro or mammalian cell-based

studies whereby experimentally applied forces were designed to mimic, but might not fully capture, the physiological condition in vivo (Abiko et al., 2015; Guilluy et al., 2011; Lessey et al., 2012; Lessey-Morillon et al., 2014). Here, we introduce the use of the *Caenorhabditis elegans* reproduction system as a model to investigate the in vivo regulation of RhoA by mechanical stretching of cells. The *C. elegans* spermatheca, a myoepithelial tube, is subjected to external forces during every embryo transit cycle (Kovacevic and Cram, 2010). Entry of the oocyte serves as a trigger by stretching of the spermathecal cells without the need for experimental manipulation of force. Further understanding of the pathways involved in stretch-mediated RhoA activation may provide insights into novel drug targets in combating various human diseases (Antoniu, 2012; Aznar et al., 2004; Chiba et al., 2010).

1.1. RhoA as a molecular switch regulating actomyosin contractility

The small GTPase RhoA is a central regulator of actomyosin-mediated contractility. RhoA is responsible for the generation of contractile forces within the cell by regulating the activity of myosin II (Chrzanowska-Wodnicka and Burridge, 1996) and formation of actin stress fibers (Watanabe et al., 1999) (Figure 1). Actin filament polymerization is facilitated by the actin nucleator and elongation factor Dia1, which is under the regulation of RhoA (Watanabe et al., 1999). On the other hand, the other direct effector of RhoA, Rho-kinase (ROCK), promotes myosin II activity by direct phosphorylation and activation of myosin light chain (MLC) (Amano et al., 1996) and/or inhibiting the function of MLC phosphatase to dephosphorylate MLC (Kimura et al., 1996). Together, these result in the generation of contractile forces at specific locations within the cell.

Although RhoA is ubiquitously expressed in the cell, precise local activation of RhoA is essential for the regulation of a specific cellular process. Using a Förster resonance energy transfer (FRET)-based biosensor, Pertz and colleagues showed that in migrating cells, active RhoA is concentrated at the edges of protrusions (Pertz et al., 2006). Hence, a higher level of regulation is required for spatial and temporal control of RhoA activity. This is achieved by three groups of proteins: 1) RhoGTPase activating proteins (RhoGAPs), 2) RhoGTPase guanine nucleotide exchange factors (RhoGEFs) and 3) RhoGTPase guanine nucleotide dissociation inhibitors (RhoGDIs) (Jaffe and Hall, 2005) (Figure 2). RhoA shuttles between the active GTP-bound and inactive GDP-bound forms. The RhoGAP family of proteins serve as a negative regulator of Rho activity by enhancing the enzymatic hydrolysis of GTP to GDP (Bernards and Settleman, 2004). On the contrary, RhoGEFs catalyze the exchange of

GDP with GTP thus promoting RhoA activation (Rossman et al., 2005). The GDI anchor proteins function to bind and sequester the inactive pool of RhoA in the cytoplasm (Garcia-Mata et al., 2011) while active RhoA is localized at the plasma membrane (Adamson et al., 1992; Lang et al., 1993).

The small GTPase RhoA is responsible for a myriad of cellular activities and its regulation is essential for proper cell function. At the organism level, mice with conditional knockout of the RhoA gene in the epidermis revealed reduced contractility and impairment in directed migration of keratinotyes (Jackson et al., 2011) while deletion of RhoA in the cerebral cortex of developing mice embryos resulted in destabilization of the actin and microtubule cytoskeleton in radial glial cells (Cappello et al., 2012). RhoA has been reported to be responsive to mechanical cues such as shear stress, intercellular tension and substrate stiffness (as reviewed in Lessey et al. (2012)). However, the mechanism behind regulation of RhoA activity in the event of the mechanical trigger is still an area of active research.
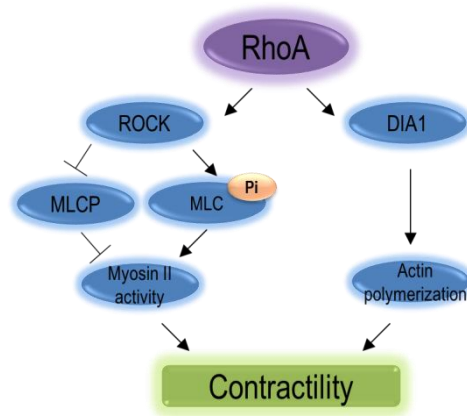
Figure 1: Schematic of RhoA-mediated regulation of actomyosin contractility.
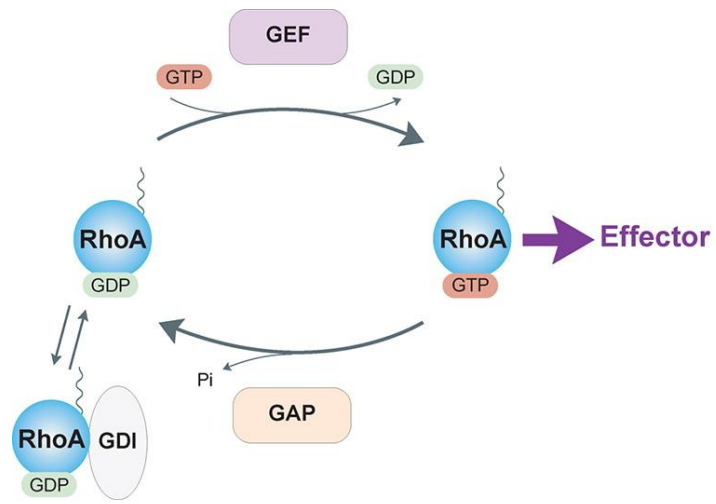
Figure 2: Schematic of the regulation of RhoA activity.

Reproduced with permission from Lessey et al. (2012).

1.2. *C. elegans* spermatheca as a model to study force-induced activation of RhoA

The Caenorhabditis elegans belongs to the phylum nematode, commonly known as the roundworm. Figure 3 depicts the anatomy of a hermaphrodite worm showing a cylindrical, unsegmented outer cuticle layer over the hypodermis. The basic anatomy of *C. elegans* includes the pharynx, intestine, gonad and nervous system. The hermaphrodite worm produces both sperm and oocytes in two symmetrical U-shaped gonad arms (Figure 4). The sperm is stored in a myoepithelial accordion-like structure termed the spermatheca while the mature oocytes are enveloped in the ovarian sheath. The spermatheca consists of 24 cells and is highly analogous to epithelial tubes in mammals such as the airway, blood vessels and salivary glands. Some common features between the spermatheca and tubular epithelial organs include the presence of cell-cell contacts, apico-basal polarity and a basally located basement membrane (Andrew and Ewald, 2010; Kovacevic and Cram, 2013; Lints and Hall, 2005).

During *C. elegans* ovulation, the oocyte in closest proximity to the spermatheca is stimulated by the major sperm protein (MSP) and undergoes maturation (Miller et al., 2001). During maturation, the nuclear envelop breaks down and the oocyte undergoes cortical rearrangement, transforming from a cylindrical to ovoid. Biochemical signals from MSP and the mature oocyte itself triggers sheath contraction and dilation of the distal (in proximity with the oocyte) end of the spermatheca (McCarter et al., 1999). The ovulation takes place when the spermatheca is pulled by the contracting sheath to envelope the most proximal oocyte. Fertilization of the oocyte happens immediately upon ovulation. The newly fertilized embryo resides in the spermatheca for several

minutes before initiation of spermathecal constriction and opening of the spermatheca-uterine (sp-ut) valve ushers the single-cell embryo into the uterus.

The morphology of the spermatheca undergoes dramatic changes during embryo transit. A spermatheca devoid of the oocyte takes the appearance of a deflated pouch with a collapsed lumen (Figure 5A, left panel). Images captured with transmission electron microscopy (TEM) revealed a convoluted membrane surface of the spermathecal cells (Figure 5B, arrows). Entry of an oocyte into the spermatheca leads to an expansion of the pouch, resulting in stretching of the spermathecal cells (Figure 5A, right panel). To facilitate embryo exit, the distal end of the spermatheca constricts in a unidirectional manner and pushes the newly fertilized embryo into the uterus. Post-embryo transit, the spermatheca collapses and awaits the next ovulation event. Precise regulation of the cyclical expansion and constriction of the spermatheca is essential for worm fertility. Overconstriction of the spermatheca leads to severing of the embryos, while lack of constriction results in embryos being trapped in the spermatheca, both resulting in embryonic lethality (Bui and Sternberg, 2002; Kariya et al., 2004; Kovacevic and Cram, 2010; Kovacevic et al., 2013; Wissmann et al., 1999).

Biochemical signaling involving the inositol 1,4,5-triphosphate (IP_3)-mediated calcium release pathway is essential for contractility of smooth muscle cells. Phospholipase C (PLC) is involved in the catalyzing the hydrolysis of phosphatidylinositol 4,5-bisphosphate (PIP_2) present on the plasma membrane to second messangers IP_3 and diacylglycerol (DAG) (Berridge and Irvine, 1989). IP3 then binds to the IP_3 receptor on the endoplasmic reticulum (ER) membrane to

stimulate calcium release (Clandinin et al., 1998). Calcium, together with calmodulin, positively regulates myosin light chain kinase (MLCK) to phosphorylate and activate myosin light chain (Rodger, 1992). In the spermatheca, knockdown and loss-of-function mutations in PLC-1 and ITR-1 (IP$_3$ receptor) revealed trapping of embryos in the spermatheca(Bui and Sternberg, 2002; Clandinin et al., 1998; Kariya et al., 2004; Kovacevic et al., 2013). Kovercic *et. al.* recently reported a unidirectional calcium wave in the spermatheca is initiated during oocyte entry travelling from the distal to proximal direction (Kovacevic et al., 2013) and this wave pattern was disrupted in mutants of the calcium signaling pathway.

In conjunction, precise regulation of spermathecal contractility is also dependent on the balance between LET-502/Rho-kinase and MEL-11/myosin light chain phosphatase (MLCP) (Wissmann et al., 1999). Although the molecular players have been well characterized, it is still unclear how the temporal control of spermathecal constriction is achieved. Furthermore, although LET-502, a direct downstream effector of RHO-1/RhoA, the contribution of RHO-1 in the spermatheca is currently unknown. In this study, we utilize the intrinsic ability of the *C. elegans* reproduction cycle to investigate the mechanism behind force-mediated regulation of a contractile event in an epithelial tube setting.
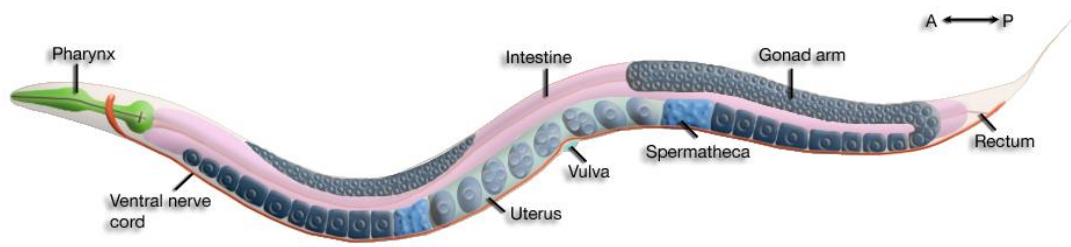
Figure 3: Anatomy of the *C. elegans* hermaphrodite.

Reproduced with permission from Wormatlas (http://www.wormatlas.org).
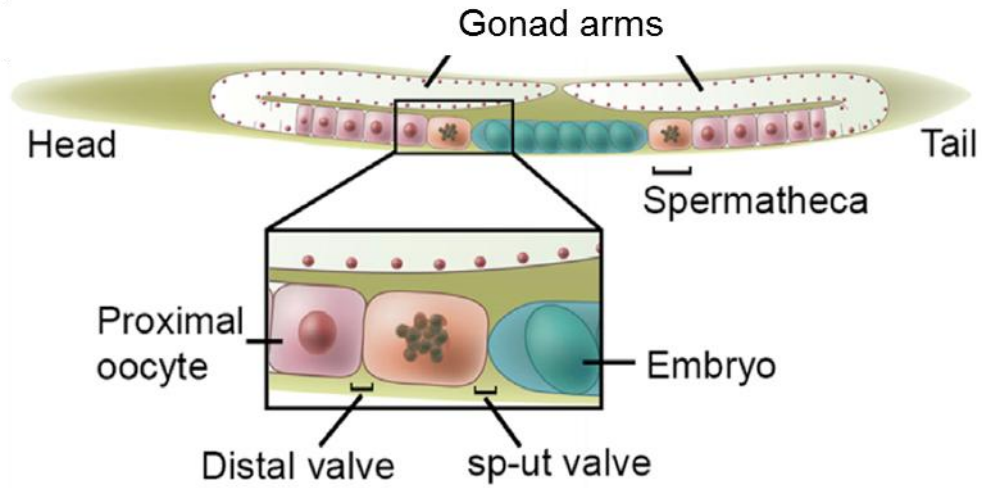
Figure 4: Illustration of the reproductive system of the _C. elegans_ hermaphrodite.

Reproduced with permission from Tan and Zaidel-Bar (2015).
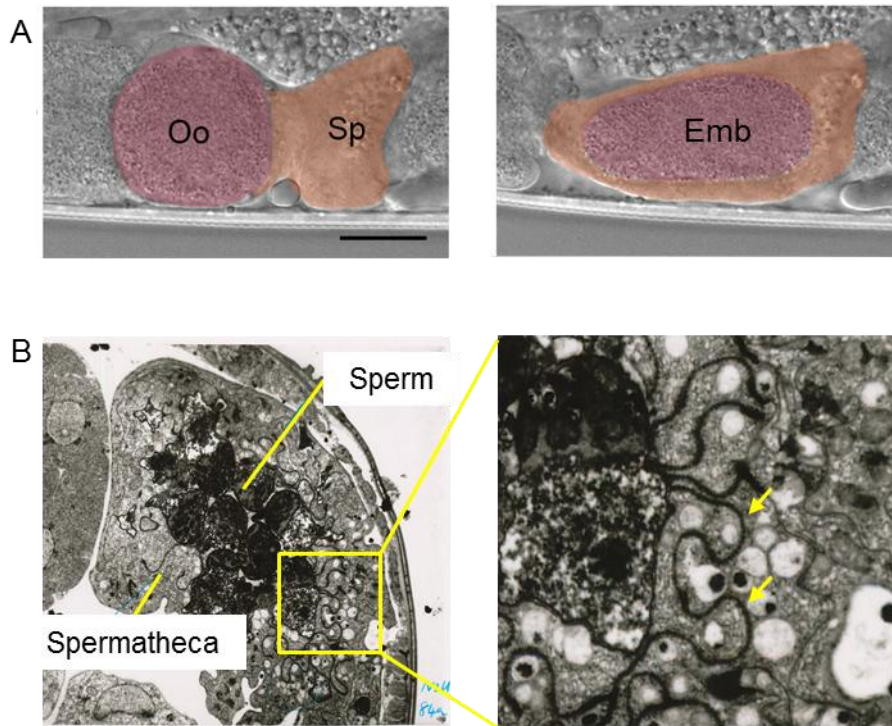
Figure 5: Changes in spermatheca morphology during embryos transit.

(A) DIC images showing a sagittal view the spermatheca in the absence and presence of an embryo. Oo: oocyte, Sp: spermatheca, Emb: embryo. Scale bar = 20 μm. Reproduced with permission from Tan and Zaidel-Bar (2015).

(B) TEM images of a transverse section of the spermatheca showing highly convoluted membranes (arrows). Reproduced with permission from www.WormImage.org[1].

1.3. Possible mechanisms for transduction of mechanical force to biochemical signals

All cells are subjected to mechanical force, whether forces are applied exogenously from the environment or internally generated by the actomyosin contractile apparatus. To adapt to the ever-changing environment, cells have evolved the ability to sense and respond to these forces. For example, fibroblast cells plated on 3D collagen matrices take on the appearance of a network of dendritic extension while cells plated on collagen-coated cover slips are well spread with prominent actin stress fibers (Grinnell et al., 2003). In recent years, there has been a rapid increase in the knowledge of the mechanisms by which cells respond to these forces. Signaling pathways involving tyrosine phosphatases, ion channels and GTPases have been identified to be initiated in response to mechanical stimuli (as reviewed in Vogel and Sheetz (2006)). The receptor-like tyrosine phosphatase α (RPTPα) has been shown to be required for force-dependent reinforcement of integrin–cytoskeleton linkages (von Wichert et al., 2003). Cell-generated traction forces mediates the opening of a mechanically-gate ion channel, Piezo1, to elicit transient Ca2+ influx to direct lineage choice in human neuronal stem cell differentiation (Pathak et al., 2014). The small GTPase Rac is inactivated in vascular smooth muscle cells and fibroblasts during equibiaxial stretch, resulting in the in the loss of lamellipodia and membrane ruffling (Katsumi et al., 2002).

External forces applied on cells through various methods such as tensile stress, shear stress, compression and experimental tether force have been reported to result in elevated RhoA activity (Lessey et al., 2012). RhoGAPs and RhoGEFs are the direct upstream regulators of RhoA activity; hence their intracellular localization could

greatly impact the pool of active of RhoA. Indeed, studies have reported the recruitment of RhoGAPs and RhoGEFs to sites of integrin- and cadherin-based adhesions in response to mechanical force (Abiko et al., 2015; Guilluy et al., 2011; Lessey-Morillon et al., 2014; Yang et al., 2011). However, the underlying mechanism behind the spatially and temporally coordinated translocation of the RhoGAPs and RhoGEFs in response to mechanical stimuli is not well understood. To the best of our knowledge, there have been no reports on RhoGEFs and RhoGAPs acting as ON and OFF switches in a molecular circuit to oscillate RhoA activity in a cyclical contractile tube setting. Here, we propose two, possibly coexisting, mechanisms which could link the sensing of mechanical force to the modulation of RhoA activity.

1.3.1. BAR-domain proteins as sensors of membrane curvature

The BIN/Amphiphysin/RVS (BAR) superfamily of protein domains is well known for its ability to remodel and tubulate the plasma membrane during clathrin-mediated endocytosis (Mim and Unger, 2012; Rao et al., 2010). There are several subfamilies of BAR domain proteins: classical BAR, Fes/CIP-4 homology-BAR (F-BAR), N-terminal amphipathic helix-BAR (N-BAR), Inverse-BAR (I-BAR), BAR-pleckstrin homology (BAR-PH) and PhoX-BAR (PX-BAR) (Frost et al., 2009). The various subfamilies of BAR domains form dimers with distinct crescent-shaped features that differ in the degree of their curvature. A high density of positive charge is found in their membrane-interacting surface to facilitate binding to the negatively-charged plasma membrane (McMahon and Gallop, 2005). Most of the BAR subfamily domains are associated with positive membrane curvature with the exception of I-BAR, which binds to negatively curved membranes (Heath and Insall, 2008; Qualmann et al., 2011; Zhao et al., 2011).

An intriguing hypothesis introduced by Peter and colleagues described the sensitivity of BAR domains to membrane curvature. They postulated BAR domains to bind with higher affinity towards curved membrane compared to flat membrane, thus acting as a sensor of membrane curvature (Peter et al., 2004). The curvature-sensing ability of BAR domains presents a mechanism for spatial and temporal regulation of protein compartmentalization, and function of BAR-domain containing proteins. A study on an N-BAR containing protein, Nesprin, successfully demonstrated the ability of BAR domain proteins to sense and be recruited to the plasma membrane when there was a change in the membrane curvature. The team reported accumulation of Nesprin at sites of high membrane curvature when cells were plated on a nanopatterned surface

with bumps or at sites of actin polymerization and membrane protrusion (Galic et al., 2012). BAR domains frequently coexist with other functional domains such as GAPs and GEFs (Peter et al., 2004). During events of mechanical stretching, the nanoscopic curves on the plasma membrane will be smoothed out. We hypothesize that the BAR domain could function as a mechanical sensor of membrane curvature for proper localization and activation of its enzymatic domain.

1.3.2. <u>Cell-matrix and cell-cell junctions as sites of mechanotransduction</u>

Integrin-based cell-matrix adhesions constitute major sites of mechanotransduction (Chen et al., 2004; Geiger et al., 2009) capable of modulating RhoA activity possibly through recruitment of RhoGAPs and RhoGEFs. Tension force applied to integrins using fibronectin-coated beads induced the recruitment of RhoGEFs GEF-H1 and LARG to focal adhesions (Guilluy et al., 2011). Furthermore, p190RhoGAP which is associated with endothelial cell-ECM adhesion, is regulated in a biphasic pattern in response to shear stress (Yang et al., 2011). Some preliminary findings indicate that similar response could be replicated at the adherens junctions. Nelson and colleagues have demonstrated that tension force on vascular endothelial (VE)-cadherin junctions led to elevated RhoA activity (Nelson et al., 2004). Recently, a RhoGEF, Solo, was identified to play a role in VE-cadherin-mediated RhoA activation during cyclic-stretch-induced reorientation of endothelial cells (Abiko et al., 2015). In *C. elegans,*the presence of β-integrin ortholog PAT-3 and adherens junctions have been observed in the spermatheca (Kovacevic and Cram, 2010; Lints and Hall, 2005). We seek to identify upstream regulators of RHO-1/RhoA that are activated in response to stretching of the cell-cell and cell-matrix contacts in the spermatheca during embryo transit.

Chapter 2:

Materials & Methods

2. Materials and Methods

2.1. *C. elegans* strains and growth conditions

Worm strains were grown on nematode growth medium (NGM) agar seeded with OP50 *Escherichia coli*. Strains were grown at 20° C unless otherwise stated. All worm strains used in this study are listed in Table 1. Mutant allele of *spv-1 (ok1498)* purchased from the *Caenorhabditis* Genetics Centre (CGC) was outcrossed two times with wild-type males to remove background mutations introduced from UV/TMP mutagenesis.

Table 1: Worm strains used in this study.

Strain	Genotype
N2	Wild-type Bristol
RZB25	*spv-1(ok1498) II outcrossed 2x*
RZB23	*spv-1(ok1498) II; msnEx23 [spv-1p::spv-1::GFP+pRF4(rol-6(su1006))]*
RZB145	*spv-1(ok1498) II; msnEx145 [sth-1p::spv-1::GFP+pRF4(rol-6(su1006))]*
RZB171	*msnEx171 [sth-1p::AHPH::GFP+pRF4(rol-6(su1006))]*
RZB173	*spv-1(ok1498) II; msnEx173 [sth-1p::AHPH::GFP+pRF4(rol-6(su1006))]*
RZB107	*spv-1(ok1498) II; msnEx107 [spv-1p::spv-1(R635K)::GFP+pRF4(rol-6(su1006))]*
RZB35	*spv-1(ok1498) II; msnEx35 [spv-1p::spv-1ΔRhoGAP::GFP+pRF4(rol-6(su1006))]*
HR863	*let-502(sb106) I*
RZB181	*spv-1(ok1498) II; let-502(sb106) I*
WS4918	*opIs310 [ced-1p::YFP::act-5::let-858 3'UTR + unc-119(+)]*
RZB180	*spv-1(ok1498) II; opIs310 [ced-1p::YFP::act-5::let-858 3'UTR + unc-119(+)]*
RZB60	*spv-1(ok1498) II; msnEx60 [spv-1p::spv-1ΔF-BAR::GFP+pRF4(rol-6(su1006))]*
RZB177	*spv-1(ok1498) II; msnEx177 [spv-1p::spv-1ΔF-BAR(PH)::GFP+pRF4(rol-6(su1006))]*
RZB202	*spv-1(ok1498) II; msnEx202[sth-1p::spv-1ΔF-BAR::GFP+pRF4(rol-6(su1006))]*
OD70	*ltIs44pAA173; [pie-1p-mCherry::PH(PLC1delta1) + unc-119(+)]*
NK358	*unc-119(ed4) III; qyIs43[pat-3::GFP + ina-1(genomic) + unc-119(+)]*
NG2517	*him-5(e1490) V; gmIs5 [ina-1::GFP + pRF4]*

2.2. Molecular cloning

All cloning reactions were performed using the Q5 High Fidelity DNA Polymerase (NEB, Ipswich, MA). Restriction enzymes, T4 DNA Ligase, T4 polynucleotide Kinase were purchased from NEB (Ipswich, MA). 2068 bp of the sequence directly upstream of the *spv-1* start site and 3781 bp of the *spv-1* genomic sequence were amplified from wild-type worm lysate. The remaining 3' end of *spv-1* was amplified using the Vidal ORF RNAi feeding clone as a cDNA template. The two fragments were combined with an intrinsic NdeI restriction site. The promoter-gene sequence was subsequently ligated into the pPD95.75 vector with a 3' GFP sequence using *PstI* and *XmaI* restriction sites. *spv-1* point mutation and deletion constructs were engineered by circle PCR cloning of the *spv-1* full length plasmid. The SPV-1 deadGAP was a substitution of an arginine residue to lysine at amino acid (AA) 635 (performed by the Mechanobiology Protein Cloning and Expression Core Facility). SPV-1ΔRhoGAP was a deletion of AA 610 to 796 and SPV-1ΔF-BAR was a truncation of AA 195 to 405. The spermathea specific promoter of *sth-1* was amplified from 2060 bp upstream of the *sth-1* start codon and replaced the *spv-1* promoter with *PstI* and *NheI* restriction sites (NEB, Ipswich, MA). Generation of the *sth-1* promoter-driven Rho-biosensor was done by cloning the AHPH anillin Rho-binding domain from plasmid pKL26 (a kind gift from Michael Glotzer, U. Chicago, USA) (Tse et al., 2012). The PH domain was cloned from the worm lysis of OD70 worm strain and inserted into the SPV-1ΔF-BAR construct to replace the F-BAR domain. The F-BAR region of SPV-1 (AA 192 – 462) was cloned into pEGFP-N1 (Clontech, Mountain View, CA) between *NheI* and *EcoRI* restriction sites. RNAi feeding clones targeting *Y37A1B.17* and *Y105E8A.25* were amplified from worm lysis at full length gene transcript sequence positions 3449-7530 bp and 37957-41416 bp

respectively and ligated into the L4440 feeding vector at the *NheI* and *XmaI* restriction sites. All cloning reactions were verified for authenticity by sequencing. Plasmids and sequencing primers were submitted to 1st BASE Pte Ltd (Singapore) for sequencing reactions. Sequencing results were verified by performing an alignment with the expected sequence using Serial Cloner software. List of cloning primers used is shown in Table 2.

Table 2: List of cloning primers used in this study.

spv-1 promoter + partial genomic sequence F	AACTGCAGTGGTCTCATCTTCTGTCGGC
spv-1 promoter + partial genomic sequence R	CAAGTCCCGCATGGATTCTG
spv-1 partial cDNA F	TCGAACTGTAACTTCCAGAGC
spv-1 partial cDNA R	TCCCCCCGGGGAAGACGTGTCGATTCAACCTTATC
spv-1 ΔRhoGAP F	TATCACATTTTTGGAATGGATCGAC
spv-1 ΔRhoGAP R	ATTTTGATGCTCTAAAAGTCCTTTC
spv-1 ΔF-BAR F	CAAACCCTGCCCACTCGAG
spv-1 ΔF-BAR R	ACTTCTACTCGGCGTATGATG
sth-1 promoter F	AACTGCAGCATTGGTAGTGTGAGCACCAC
sth-1 promoter R	CTAGCTAGCGTTGCTCTAGCACAAAAGACTC
spv-1 Δspv-1 promoter F	CTAGCTAGCATGTCGTCGACGAGCAGTATATG
spv-1 Δspv-1 promoter R	AACTGCAGGCATGCAAGCTTATTTC
AHPH F	TCAAGTCGACGCAATGGATGACGATGCAACAACAC
AHPH R	TGGCCAATCCCGGGGCTGATTAACAATCGGATTTCTC
PH F	CACGGGCTCCAGGATGAC
PH R	CTTCTGCCGCTGGTCCATG
F-BAR F	CTAGCTAGCGATGAGCACGCTGGGTCGCTGG
F-BAR R	GGAATTCGCTCGTCAATTGAGCGATCCG
Y37A1B.17 F	CTAGCTAGCATGCTCTTACCAACTCGGCG
Y37A1B.17 R	CCCCCCGGGCACTGGACGAATCGCTGTCG
Y105E8A.25 F	CTAGCTAGCGCTCTACCTAATGGAAAAACGTC
Y105E8A.25 R	CCCCCCGGGATCGATTCAACGGAATAACTCTGG

2.3. Genotyping PCR

Worms were lysed by incubating in lysis buffer (50 mM KCl, 10mM Tris pH8.2, 2.5 mM $MgCl_2$, 0.45% Tween-20,6 mg/ml Protease K) at 60 °C for 60 min. To confirm the identity of mutant worms, two PCR reactions were performed using 1) forward and reverse primers flanking the deletion site (Primers 1 and 2) and 2) forward primer in the deletion site paired with the reverse primer flanking the deletion site (Primers 2 and 3) (Figure 6). The genotyping primer sequences are listed in Table 3.
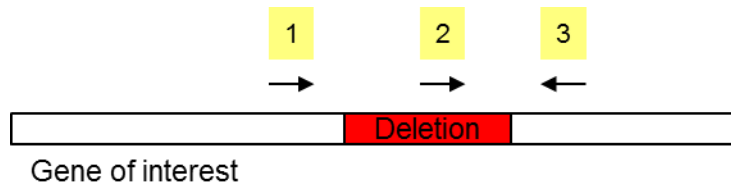
Figure 6: Schematic of the location of genotyping primers.

Table 3: List of genotyping primers used in this study.

spv-1 (ok1498) F (flaking deletion site)	AGGAGCTCTTCCAGACACCA
spv-1 (ok1498) R (flaking deletion site)	ATCGGTGTTGGCTCTACGTC
spv-1 (ok1498) F (within deletion site)	CAGAATGTTGTTCTGCACAAGC
rhgf-1 (ok880) F (flaking deletion site)	TGTAGGGATGCTATCTGGGG
rhgf-1 (ok880) R (flanking deletion site)	CGTAGTTTGCGCACTCACATC
rhgf-1 (ok880) F (within deletion site)	GACGAAAGTGATATTGGTGACAG

2.4. Generation of transgenic animals

2.4.1. Genetic cross

L4 hermaphrodites were incubated at 30° C for 5 h to induce the formation of male worms. Males were identified and confined with hermaphrodites of the desired strain (P0 generation) for 24 h to encourage mating. Successfully mated P0 hermaphrodites will give rise to heterozygous F1 progeny with a 50% male population. The F1 progenies were isolated and allowed to propagate. F2 progenies homozygous for the desired genotype were identified by genotyping.

2.4.2. Injection

Transgenic worms expressing the Rho-biosensor and various forms of the SPV-1 constructs were generated by injection. The injection mix contained 100 ng/μl pBluescript as carrier DNA, 20 ng/μl *rol-6 (su1006)* co-injection marker and 10 ng/μl of plasmid carrying the construct of interest. Worms were mounted on desiccated 3% agarose pads coated with mineral oil (Sigma-Aldrich, St. Louis, MO). The injection needle was prepared from a glass capillary (Narishige, Japan) using a P-97 Flaming/Brown Micropipette Puller (Sutter Instruments, Novato, CA). The microscope setup is as follow: Nikon Ti microscope (Nikon, Tokyo, Japan), S Plan Fluor 40x objective (Nikon, Tokyo, Japan), Eppendorf PatchMan NP2 micromanipulator (Eppendorf, Hamburg, Germany). The mixture was injected into the gonad of young adult hermaphrodites using a nitrogen gas-powered pump on the injector. Injected worms were transferred onto NGM plates with a drop of M9 buffer (2.2 mM KH_2PO_4, 4.2 mM Na_2HPO_4, 85.6 mM NaCl, 1 mM $MgSO_4$) to aid worm recovery. The progenies of the injected worms (F1 generation) showing a roller phenotype were isolated onto individual plates. Each P1 worm that successfully

transferred the roller phenotype to subsequent generations was considered as an independent strain.

2.5. Progeny test

Adult worms were placed for several hours on NGM plates seeded with OP50 bacteria to allow them to lay embryos. Next, the adult worms were removed and the number of embryos on the plates was counted. The embryos were incubated for 24 h at 20° C, after which the number of hatched progenies was scored. Embryonic lethality was calculated from the following formula:

$$\left(\frac{total\ number\ of\ embryos - number\ of\ hatched\ progenies}{total\ number\ of\ embryos}\right) \times 100\%$$

2.6. RNAi knockdown by feeding

RNA interference (RNAi) feeding clones were mostly from Vidal (OpenBioSystems) and Ahringer (Source BioScience) libraries (Table 4). RNAi clones for *rhgf-1*, *rhgf-2*, *pix-1* and *unc-73* were kindly provided by Erin Cram (Northeastern University, Boston, MA), *par-5* was a kind gift from Takao Inoue (National University of Singapore). Clones targeting *Y37A1B.17* and *Y105E8A.25* were generated in-house (refer to Section 2.2). To induce the transcription of dsRNA in the feeding clones, bacteria was plated on isopropyl β-D-1-thiogalactopyranoside (IPTG) plates, which were prepared by supplementing NGM agar plates with 50 µg/ml Carbenicillin and 1 mM IPTG. RNAi feeding bacteria was inoculated in LB broth supplemented with 100 µg/ml Ampicillin. 50-200 µl of the overnight bacteria culture was seeded onto the IPTG plates and incubated overnight at room temperature. Worm strains of interest were transferred onto IPTG plates seeded with bacteria and incubated at either 20 or 25° C for 24-72 h. Bacteria carrying the L4440 empty vector were used as a negative control whereas *par-5* and *rho-1* targeting clones were positive controls for experiments involving embryonic lethality and spermathecal contractility respectively.

Table 4: List of RNAi clones from the Vidal and Ahringer libraries.

RNAi clones from the Ahringer library	RNAi clones from the Vidal Library
pac-1	*ect-2*
F23H11.4	*unc-89*
rlbp-1	*cgef-1*
R02F2.2	*F52D10.6*
exc-5	*tag-218/ephx-1*
cgef-2/tiam-1	*T04C9.1*
tag-77	*rga-5*
	rrc-1
	tag-341
	tag-52
	Y95B8A.12
	vav-1
	uig-1

2.7. In vitro RhoGAP activity assay

A bacterially produced protein containing the C terminus of SPV-1 (AA 584 − 966) inclusive of the RhoGAP domain was prepared by the Protein Production Platform (Nanyang Technological University, Singapore). Briefly, The RhoGAP domain, positions 1750 − 2898 bp of *spv-1* cDNA, was cloned into the pNIC28-Bsa4 vector harboring the His-TEV tag and transformed into BL21 for protein expression. Protein was purified using Ni-NTA column followed by gel filtration chromatography.

RhoGAP activity of the recombinant SPV-1 fragment was evaluated with the in vitro RhoGAP assay (Cytokskeleton) according to manufacturer's protocol. Briefly, the GAP protein was incubated with RhoA and excess GTP for 20 min at 37 °C. The catalytic domain of p50 RhoGAP was used as a positive control. Release of inorganic phosphate (P_i) was visualized by the addition of CytoPhos reagent and measured at A_{650} using a spectrophotometer (Tecan).

2.8. Bioinformatics

Protein domains for SPV-1 were identified by conducting a conserved domain search (Marchler-Bauer et al., 2011). Paircoil2 was utilized to predict the presence of coiled-coil regions (McDonnell et al., 2006). Structure predictions for full-length and the F-BAR domain of SPV-1 were performed using Phyre2 (Kelley and Sternberg, 2009) and I-TASSER (Roy et al., 2010) respectively. DELTA-BLAST was used to identify orthologs of SPV-1 (Boratyn et al., 2012). Multiple sequence alignment of the F-BAR region across the metazoan phylum was performed with T-coffee (Notredame et al., 2000) and visualized with Jalview (Waterhouse et al., 2009). Phylogenetic analysis of the F-BAR sequences was performed with PHYLIP-NEIGHBOR (MPI Bioinformatics Toolkit) (Biegert et al., 2006) and an unrooted phylogenetic tree was drawn with Dendroscope (Huson and Scornavacca, 2012).

2.9. Cell culture

HeLa cells were cultured in Dulbecco's Modified Eagle's Medium (DMEM) (Invitrogen) supplemented with 10% Fetal Bovine Serum (FBS) (Invitrogen) and 1% Penicilin-Streptomycin (Invitrogen) and incubated in 37° C at 5% CO_2 atmosphere. Cells for imaging were seeded on 30 mm glass coverslip and transfected with 1 µg of F-BAR::GFP plasmid using Lipofectamine 2000 (Invitrogen) in accordance to the manufacturer's instructions. Cells were imaged 24 h post transfection in DMEM.

Cell membrane was stained with a membrane dye DiI 561by incubating cells in 1:1000 dilution of dye:PBS for 5min, followed by three 5 min wash in PBS. Trypsinization was performed by removing the DMEM and replacing with Trypsin (Invitrogen). The trypsin reaction was quenched with excess DMEM.

2.10.   Image acquisition

2.10.1. <u>Microscope setup</u>

Images in Figures 5A, 7B, 8, 10A, 11B, 12A, 13D, 14A, 23 DIC panel, 24, 25 and 29 were acquired with a Nikon Ti microscope (Nikon, Tokyo, Japan) mounted with a differential interference contrast (DIC) 1.40NA oil condenser (Nikon, Tokyo, Japan) and a charged-coupled device (CCD) camera (CoolSNAP HQ2, Photometrics, Tucson, AZ), using either 20x S Plan Fluor 0.45NA air objective or 60x Plan-Apo 1.40NA oil objective (Nikon, Tokyo, Japan). The remaining images were captured on a spinning disk confocal microscope composed of Nikon Ti microscope base (Nikon, Tokyo, Japan) with CSU-X1 spinning-disk confocal head (Yokogawa Corporation, Tokyo, Japan), DPSS-Laser (Roper Scientific, France) at 491nm excitation wavelength, and an Evolve Rapid-Cal electron multiplying charged-coupled device (EMCCD) camera (Photometrics, Tucson, AZ) using either 60x or 100x Plan-Apo 1.40NA oil objectives (Nikon, Tokyo, Japan). Metamorph software (Molecular Devices, Sunnyvale, CA) was used to control the acquisition. All imaging was performed at 20 °C.

2.10.2. <u>Preparation of sample slides</u>

For preparation of embryo mounts, gravid hermaphrodites were dissected in M9 buffer to release the embryos. Embryos were transferred onto a 3% agarose pad on a glass slide. To image embryo transit, a single adult hermaphrodite was placed on 10% agarose with a drop of M9 buffer. A glass coverslip was placed on top of the sample and the space between the coverslip and slide was infused with M9 buffer. The edges of the coverslip were sealed with wax to prevent sample desiccation.

2.10.3. Image analysis and quantification

Images and movies were analyzed using ImageJ (NIH). Quantification of the constriction magnitude was performed by calculating the ratio of the measured width between distal and proximal ends of the spermatheca during embryo transit. Valve-to-valve time was the quantification of time elapsed between the closure of the distal valve and opening of the sp-ut valve. Measurement of embryo cross-section area was done by manually tracing the perimeter of the embryos imaged at a medial plane. Quantification of the embryo axial ratio was obtained by the ratio between measurements of the long over the short axis. Intensity changes of the Rho-biosensor in the spermatheca were measured by quantifying the mean intensity of the whole spermatheca at the middle focal plane across time and normalized to the intensity at the first time point. Membrane and cytoplasm intensities for SPV-1 localization were obtained by manually tracing along the cell edge or cytoplasm. Membrane-to-cytoplasm ratio of SPV-1 localization was the ratio between the mean intensities for the line traces at the cell edge and cytoplasm. Data sets were statistically analysed (two-tailed unpaired t test for Figures 10B,C, 11A and 15B; ordinary one-way ANOVA-Tukey's multiple comparison for all other data sets) and drawn using Prism 6 (Graphpad).

Chapter 3:

Results

3. <u>Results</u>

3.1. RHO-1 is a key regulator of spermathecal contractility

The spermatheca undergoes periodic constriction and relaxation during embryo transit events. The presence of NMY-1/non-muscle myosin II (Kovacevic et al., 2013) and circumferential actin bundles visualized by YFP::ACT-5 (Figure 7A) as well as phalloidin staining (Kovacevic and Cram, 2010) in the spermathecal cells suggest the actomyosin machinery is the driving force of spermatheca contractililty. Furthermore, the well-established antagonistic functions of LET-502/Rho-kinase and MEL-11/Myosin light chain phosphatase in maintaining the balance between constriction and relaxation in the spermatheca (Wissmann et al., 1999), suggests the involvement of RHO-1 as an upstream regulator in the temporal regulation of spermathecal constriction. However, since the contribution of RHO-1 in spermathecal contractility has not been reported, we directly tested the involvement of RHO-1 during embryo transit by performing a partial knockdown of RHO-1 by RNAi feeding. In a mock RNAi knockdown in the wild type background, the representative images showed the oocyte fully entered into the spermatheca (indicated as time = 0) and resided in the spermatheca for 213 sec (mean ± SEM = 244.3 ± 11.8, n = 12) (Figure 7B). This was followed by the opening of the sp-ut valve and initiation of embryo exit. The newly fertilized embryo completed its exit from the spermatheca after 345 sec. A 36 h knockdown of RHO-1 resulted in complete loss of spermathecal constriction leading to multiple embryos trapped in the spermatheca (Figure 7B, n = 14). The embryos failed to exit the spermatheca in the 30 min imaging timeframe. Retaining of embryos in the spermatheca during loss of RHO-1 phenocopies the loss of NMY-1 and LET-502 (Kovacevic et al., 2013; Wissmann et al., 1999). Loss of RHO-1 likely hindered the activation of downstream LET-502 and phosphorylation of NYM-1, hence

interrupting spermathecal constriction and leading to defective embryo exit from the spermatheca.

A   YFP::act-5

Wild-type

B

| | Oocyte maturation | Complete ovulation | Initiate embryo exit | Complete embryo exit |

Control

Oo   Sp

60 sec | 0 sec | 213 sec | 345 sec

rho-1 (RNAi)

Embryos trapped in the spermatheca

0 sec | 600 sec | 1200 sec | 1800 sec
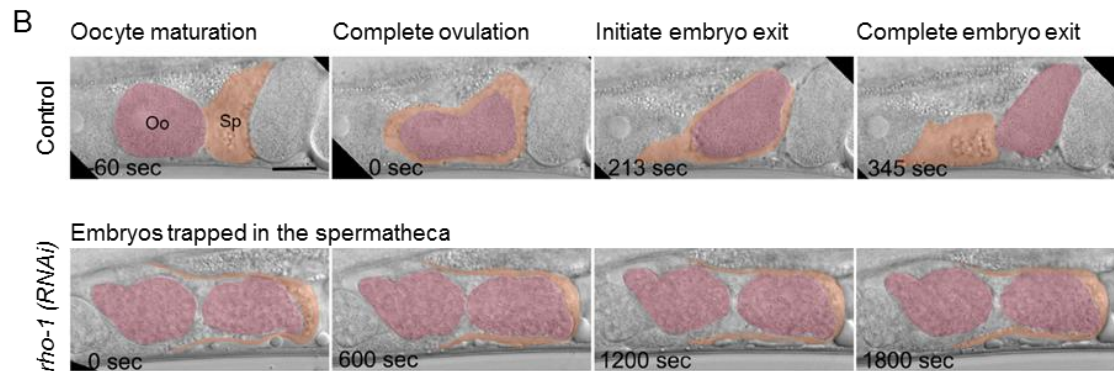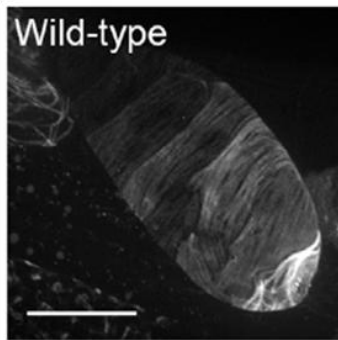
Figure 7: RHO-1 is essential for spermathecal constriction.

(A) Circumferential actin bundles in the wild-type spermatheca visualized by YFP::ACT-5. Scale bar = 20 μm.

(B) Effects of RHO-1 knockdown in the wild-type spermatheca. Representative images of an embryo transit event taken from L4440 (negative control) and *rho-1 (RNAi)* treated worms. In *rho-1* knockdown, embryos (highlighted in pink) remain in the spermatheca (highlighted in orange) throughout the 30 min imaging period. n ≥ 12, Oo: oocyte, Sp: spermatheca. Scale bar = 20 μm.

Reproduced with permission from Tan and Zaidel-Bar (2015).

3.2. Identification and characterization of a RhoGAP involved in spermathecal constriction

3.2.1. Loss of SPV-1 results in spermathecal overconstriction

To identify upstream regulators of RHO-1 activity in the spermatheca, we performed a candidate screen of RhoGAPs in the *C. elegans* genome by RNAi feeding. The RhoGAP candidates tested are listed in Table 5. We reasoned that if spermathecal functions were perturbed, the resulted embryos would take on an irregular appearance as well. For all the candidates screened, *temporary assigned gene (tag)-341* was the only gene that gave embryos of abnormal morphology when knocked down by RNAi feeding at 25 °C for 48 h (Figure 8). The arrows indicate elongated embryos while the arrowhead points to a round embryo. We have since renamed *tag-341* to *spermatheca physiology variant (spv)-1*.

To further characterize the contribution of *spv-1* in spermathecal constriction, a deletion allele, *spv-1 (ok1498)*, was obtained from the CGC. The *spv-1* gene consists of 18 exons and 17 introns (Figure 9A). The 577 bp frame shift deletion mutant *spv-1 (ok1498)* lacks part of the RhoGAP sequence. Genotyping was performed by using a combination of two primers flanking the deletion site (Figure 9A, inset, primers 1 and 3) and one internal with one external primer (Figure 9A, inset, primers 2 and 3) to confirm the identity of the mutant worms. Using primers flanking the deletion region (primers 1 and 3), PCR amplification of the wild type worm gave a 2991 bp band whereas a 577 bp deletion in the mutant allele resulted in a lower molecular weight 2414 bp band (Figure 9B, left panel). Amplification using primers 2 and 3 resulted in a 2327 bp band for the wild-type allele and the absence of a band confirms the

absence of a wild-type allele in the mutant (Figure 9B, right panel). These results confirmed the identity of the *spv-1 (ok1498)* deletion allele. Since the mutation was generated by UV/TMP irradiation, we outcrossed the mutant allele twice with wild-type males to remove background mutations. The twice-outcrossed *spv-1 (ok1498)* allele was used for further characterization.

We analyzed embryo transit events in wild-type and *spv-1 (ok1498)* mutants using differential interference contrast (DIC) microscopy (Figure 10A). Complete ovulation, defined by the complete closure of the distal valve upon oocyte entry into the spermatheca, is referred to as time 0. The embryo residence time in the spermatheca termed 'valve-to-valve' time is defined as the time elapsed between closure of the distal valve and opening of the sp-ut valve. In wild-type worms, embryos resided in the spermatheca for 247.2 (mean) $\pm$ 11.61 (SEM) sec before the spermatheca constricted and propelled the embryo into the uterus (n = 23) (Figure 10A,B). This was significantly different (p<0.0001) from the 94.50 $\pm$ 10.29 sec of valve-to-valve time for *spv-1 (ok1498)* (n = 28) (Figure 10A, B). To quantitatively assess the magnitude of spermatheal constriction, we measured the width at its distal (W_1) and proximal (W_2) quarters prior to initiation of embryo exit and calculated the W_1/ W_2 ratio. *spv-1 (ok1498)* (n = 28) showed a 31% increase in constriction magnitude compared to wild-type spermatheca (n = 23) during embryo transit (Figure 10B). To further validate that the difference in constriction magnitude was contributed by a stronger distal constriction in *spv-1 (ok1498)* mutant, we plotted the individual spermatheca width for both distal and proximal ends (Figure 10C). As expected, the proximal width (W2) did not differ significantly between wild-type (23.96 $\pm$ 0.6) and mutant (23.55 $\pm$ 0.5) worms whereas the distal width was

significantly reduced in the mutant.(p<0.0001) (Figure 10C).Taken together, quantifications of valve-to-valve time and constriction magnitude suggested that premature exit of the embryo in the *spv-1 (ok1498)* mutants resulted from the precocious and excessive constriction of the spermathecal cells. Hence, we followed the changes in constriction magnitude over the course of a single embryo transit event in both wild-type and mutant worms (Figure 10D). The wild-type spermatheca showed slightly elevated W_1/ W_2 ratio during the initial phase of embryo transit that gradually plateaued and decreased slightly prior to sp-ut valve opening (n = 7). On the contrary, the width of the spermatheca for *spv-1 (ok1498)* mutants decreased immediately upon completion of ovulation and continued to decrease until initiation of embryo exit (n =7). This further corroborated the finding that loss of *spv-1* resulted in premature and excessive spermathecal constriction.

An increase in constriction magnitude could be expected to lead to accelerated embryo exit time, defined by the time from initiation of embryo exit from the spermatheca to completion of exit into the uterus. However, the mean embryo exit time between wild-type (92.35 ± 12.84, n = 23) and *spv-1 (ok1498)* mutant (115.8 ± 13.84, n = 24) was not significantly different (Figure 11A). We attributed this to the spermatheca behaving like a vice during constriction in the *spv-1(ok1409)* mutants and preventing embryo exiting the spermatheca and sometimes completely severing the embryos (Figure 11B).

Table 5: List of RhoGAP-containing genes knocked down by RNAi feeding.

Gene Name
F23H11.4
pac-1
rga-5
rlbp-1
rrc-1
T04C9.1
tag-341/spv-1
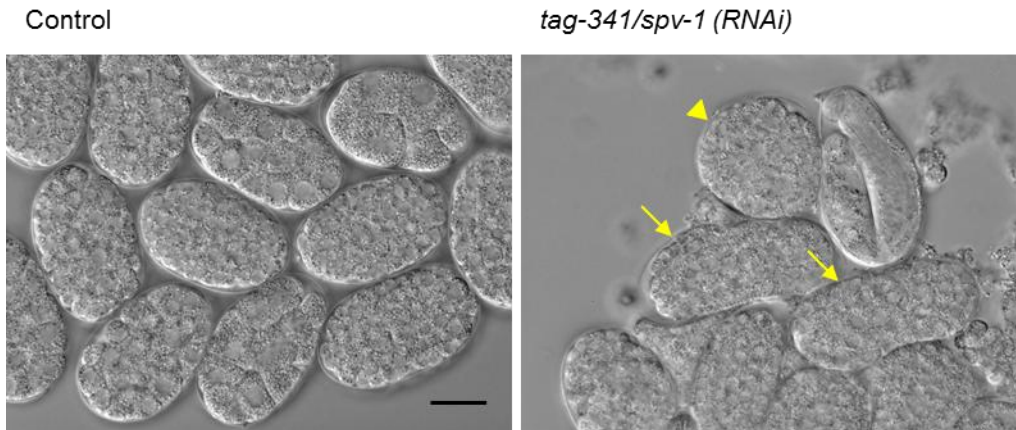
Figure 8: Loss of SPV-1 results in embryos of irregular geometry.

Wild type worms treated with mock RNAi shows stereotypical embryo shape (left panel). Embryos from *spv-1* RNAi treated worms have aberrant morphology (right panel). Arrows indicate elongated embryos while arrowhead points to a round embryo. Scale bar = 20 μm.

Reproduced with permission from Tan and Zaidel-Bar (2015).
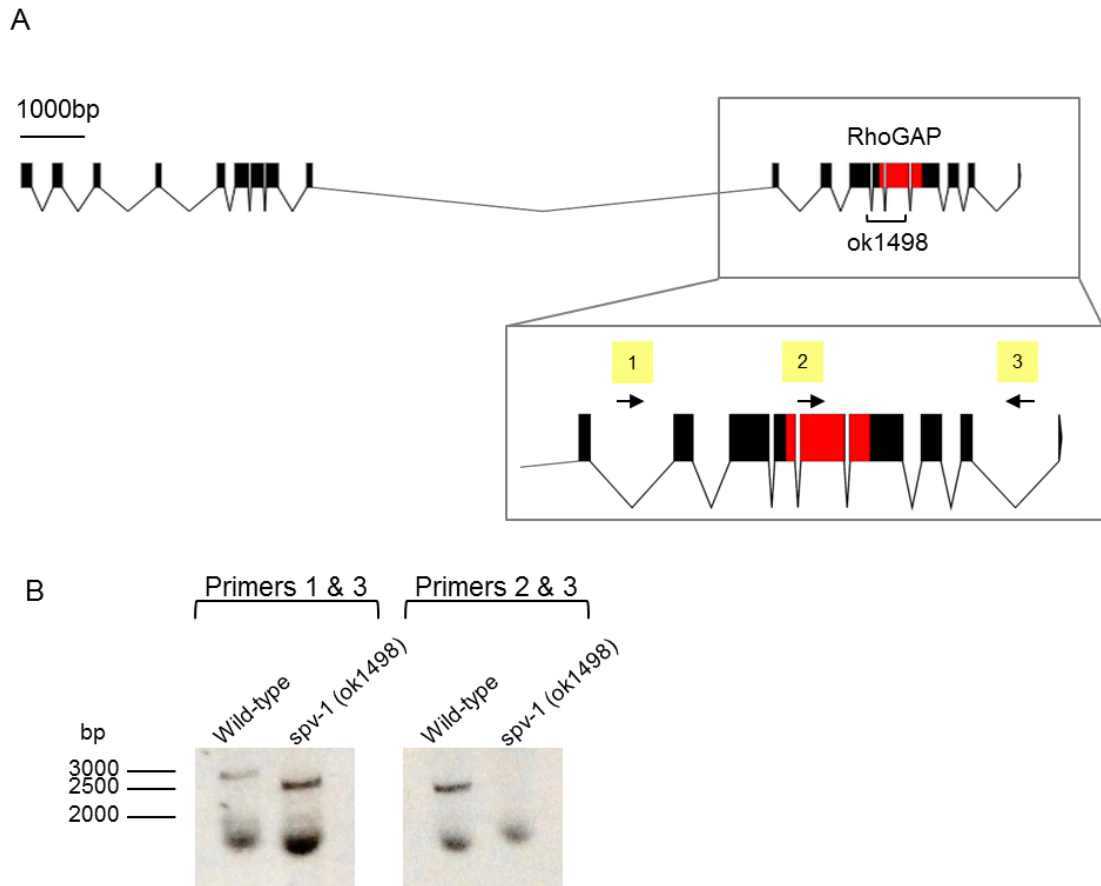
Figure 9: Genotyping of the *spv-1 (ok1498)* mutant allele.

(A) Gene structure of the *spv-1* locus. Rectangles and lines represent exons and introns respectively. DNA sequence coding for the RhoGAP domain is marked in red. The deletion region in *spv-1 (ok1498)* is indicated by a bracket. Inset shows the location of genotyping primers.

(B) Gel image of *spv-1 (ok1498)* genotyping. External primers (1 and 3) gives a 2991 bp and 2414 bp band for wild-type and *spv-1 (ok1498)* mutant respectively. The internal and external primer paring (2 and 3) resulted in a 2327 bp band for wild-type and no amplification for the mutant.
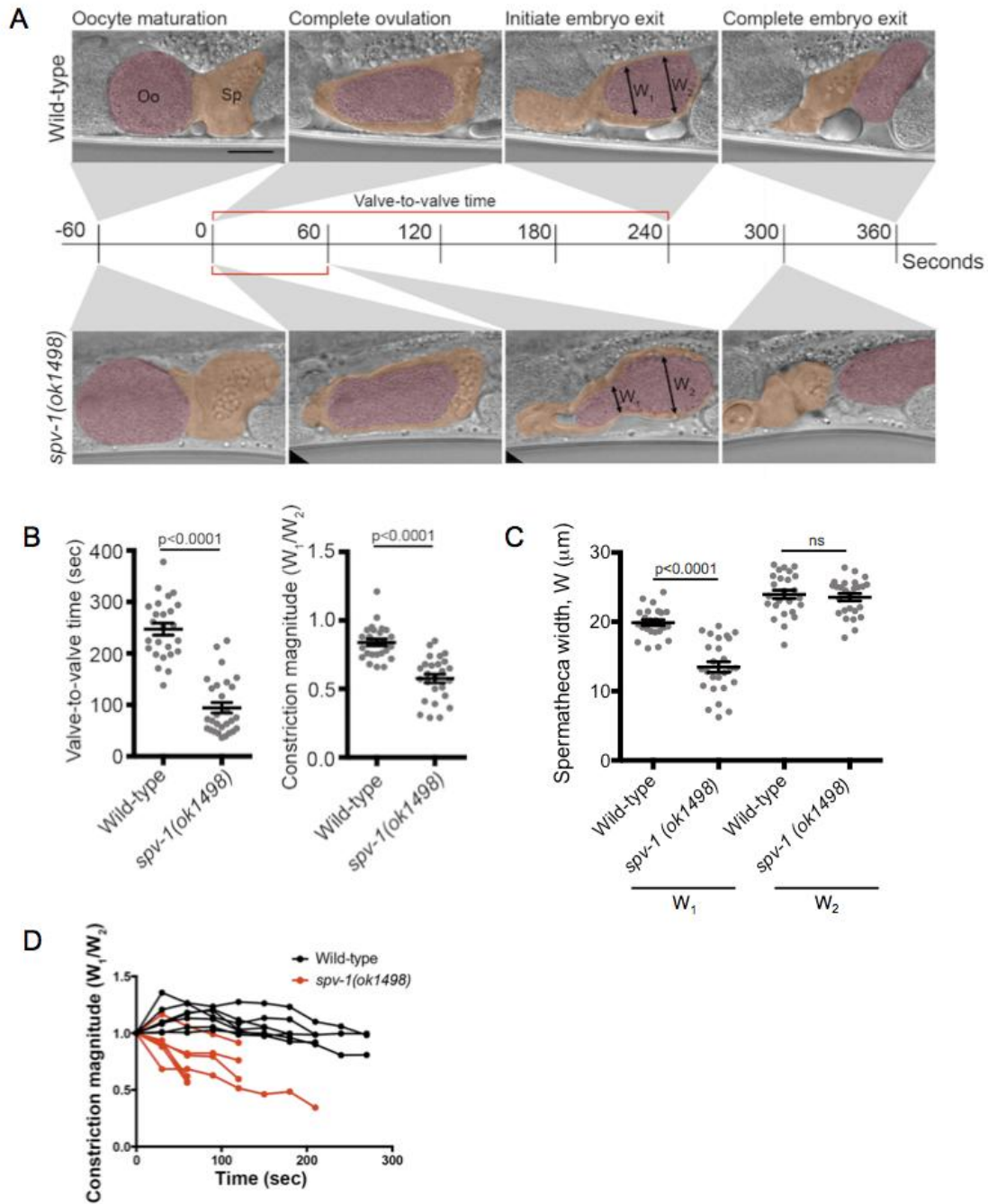
Figure 10: SPV-1 is a negative regulator of spermathecal contractility.

(A) Representative images of embryo transit events in wild-type and *spv-1 (ok1498)* mutants. Complete ovulation is defined by the closure of the distal valve following ovulation. Initiation of embryo exit is defined by the opening of the sp-ut valve. Valve-to-valve time represents the elapsed time between complete ovulation and initiation of embryo exit. W_1 and W_2 represent the width of the spermatheca at the first and last quarter respectively. Oo: oocyte, Sp: spermatheca. Scale bar = 20 μm.
(B) Quantifications of valve-to-valve time and constriction magnitude in wild-type and *spv-1 (ok1498)* mutant animals. Each data point (grey dot) is a single embryo transit event. Data are represented by mean ± SEM with $n \geq 23$ for each worm strain analyzed. Statistical comparisons were performed using two-tailed unpaired t test.

(C) Quantifications of spermatheca width at the distal (W1) and proximal (W2) ends of wild-type and *spv-1 (ok1498)* mutant animals. Data are represented by mean ± SEM with n ≥ 23 for each worm strain analyzed. Statistical comparisons were performed using two-tailed unpaired t test. Data points were used to quantify the constriction magnitude in (B).

(D) Quantification of the dynamic changes in spermatheca constriction magnitude during embryo transit in wild-type and *spv-1(ok1498)* mutants. Measurements were taken at 30 sec intervals from closure of the distal valve to opening of the sp-ut valve. Each line represents one embryo transit event. N = 7 for each strain.

Panels A, B and D are reproduced with permission from Tan and Zaidel-Bar (2015).
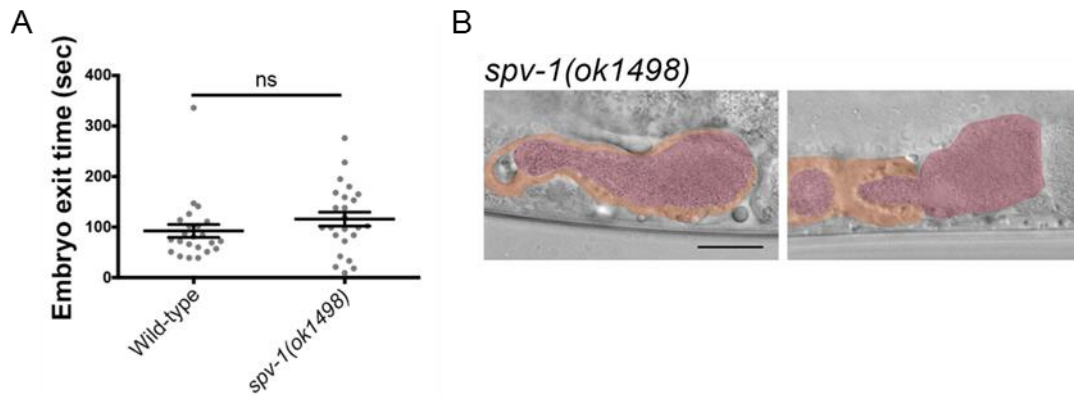
Figure 11: Defective embryo exit in *spv-1 (ok1498)* animals.

(A) Quantification of embryo exit time (the time taken from opening of the sp-ut valve till complete exit of the embryo from the spermatheca) in wild-type and *spv-1(ok1498)* worms. Each data point (grey dot) is a single embryo transit event. Data are represented by mean ± SEM with n ≥ 23 for each worm strain analyzed. Statistical comparisons were performed using two-tailed unpaired t test.
(B) Representative images of hyperconstricted spermatheca in *spv-1(ok1498)* worms demonstrating how an embryo can be trapped like in a vise (left) and severed (right). Scale bar: 20 μm

Reproduced with permission from Tan and Zaidel-Bar (2015).

3.2.2. Loss of *spv-1* results in misshapened embryos and increases lethality

As a consequence of the excessive constriction in *spv-1* loss-of-function worms, we observed deformation and pinching of the embryos during the ovulation process (Figure 11B). This resulted in the formation of embryos of aberrant morphology (Figure 8, Figure 12A). The stereotypical geometry of wild-type embryos is an ellipsoid with mean axial ratio and area of 1.69 and 1372 μm^2 respectively (n = 50) (Figure 12B). On the contrary, *spv-1 (ok1498)* and knockdown of *spv-1* by RNAi resulted in a large distribution of axial ratio and area size ranging from 1.00 – 2.38 and 379.4 – 1866.8 μm^2 respectively (n > 50) (Figure 12B). In addition, loss of *spv-1* also resulted in embryonic lethality of 41% and 50% for *spv-1 (ok1498)* and *spv-1 (RNAi)* respectively (Figure 12C). Interestingly, we observed a bias for developmental arrest for embryos that fall below a critical axial ratio of 1.69 (Figure 12B). Although most of the small embryos probably failed to hatch due to lost of cytoplasmic content, rounder than normal embryos that fell within the wild-type range of area (yellow band) showed a higher percentage of lethality that was not observed for embryos that were abnormally elongated. This hinted at the possibility that embryonic lethality could be contributed by the embryo morphology.
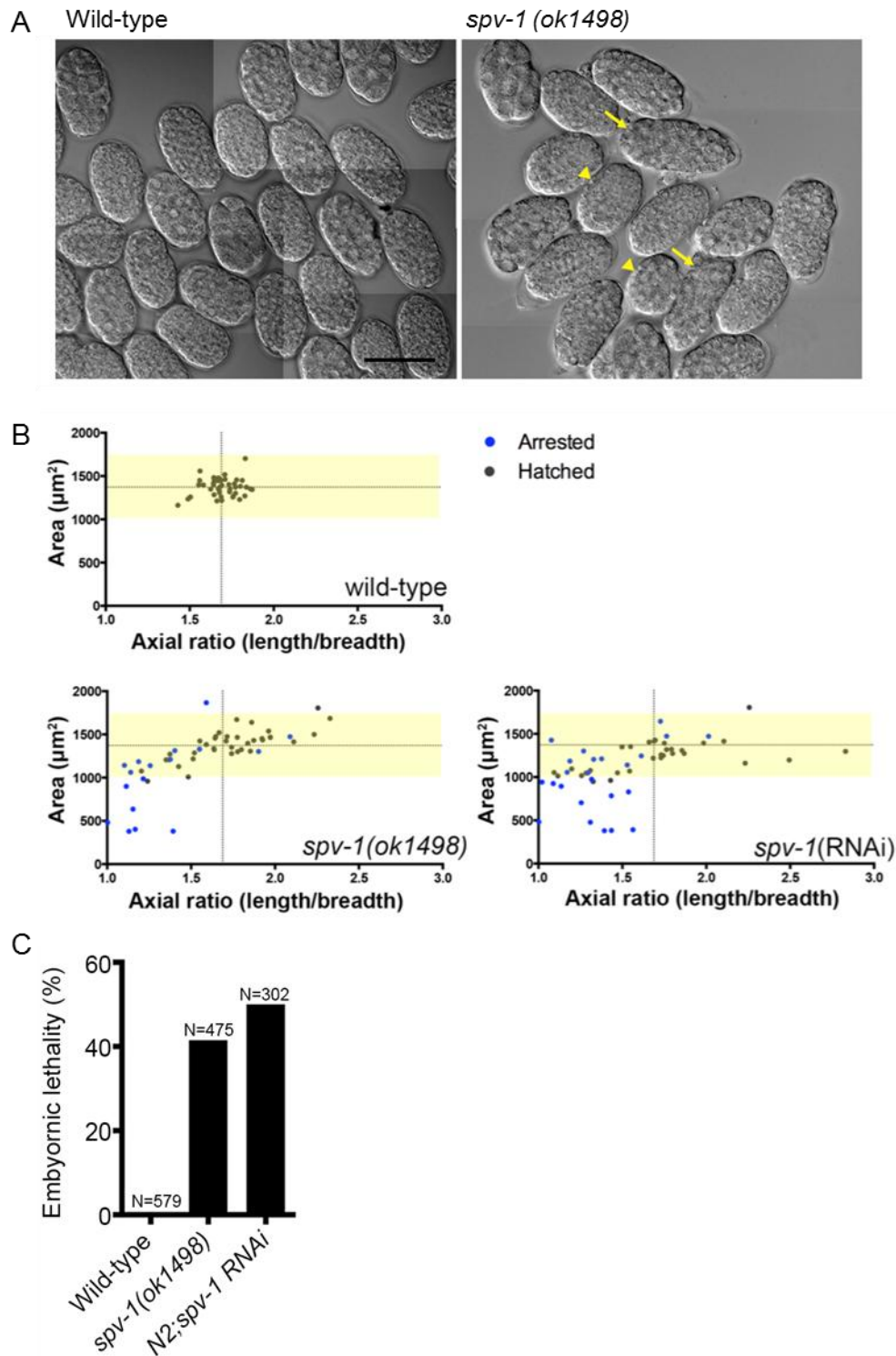
Figure 12: SPV-1 contributes to formation of stereotypical embryo shape and embryonic viability.

(A) Wild-type and *spv-1 (ok1498)* mutant embryos. Arrows and arrowheads indicate elongated and round embryos respectively. Scale bar = 50 μm.
(B) Comparison of the area and axial ratio distribution between wild-type, *spv-1(ok1498)* mutant and *spv-1* knock-down embryos. Dotted lines represent the mean values for the x- and y-axis for the wild-type embryos, and the region highlighted in

52

yellow marks the wild-type range of embryo area. Each dot represents a single embryo with blue and grey dots indicating embryos that arrested and hatched respectively. N ≥ 50 for each strain quantified.

(C) Quantification of embryonic lethality in wild-type, *spv-1 (ok1498)* and *spv-1 (RNAi)* treated worms. N represents the number of embryos scored.

Reproduced with permission from Tan and Zaidel-Bar (2015).

3.2.3. SPV-1 is expressed exclusively in the spermatheca

Given the apparent function of SPV-1 in the spermatheca, we next proceeded to determine its expression pattern. We engineered a translational fusion construct of SPV-1::GFP driven by the *spv-1* endogenous promoter. SPV-1::GFP was observed exclusively in the spermatheca (Figure 13A, arrowhead). It is worth noting that the prominent fluorescence in the worm intestine is a result of gut granule autofluorescence (Figure 13A, arrow). Importantly, expression of the SPV-1::GFP fusion protein in the *spv-1 (ok1498)* background successfully rescued all the mutant phenotypes: constriction magnitude and valve-to-valve time was restored to wild-type levels (n = 23) (Figure 13B), embryonic lethality was eliminated (n = 370) (Figure 13C), and embryo geometry was restored to wild-type dimensions (Figure 13D). Thus, we concluded that the fusion protein is functional. SPV-1 expression observed in the spermatheca was consistent with the overconstriction phenotypic in worms lacking *spv-1*. Importantly, we did not detect SPV-1 expression in the embryos (Figure 13A, asterisk).
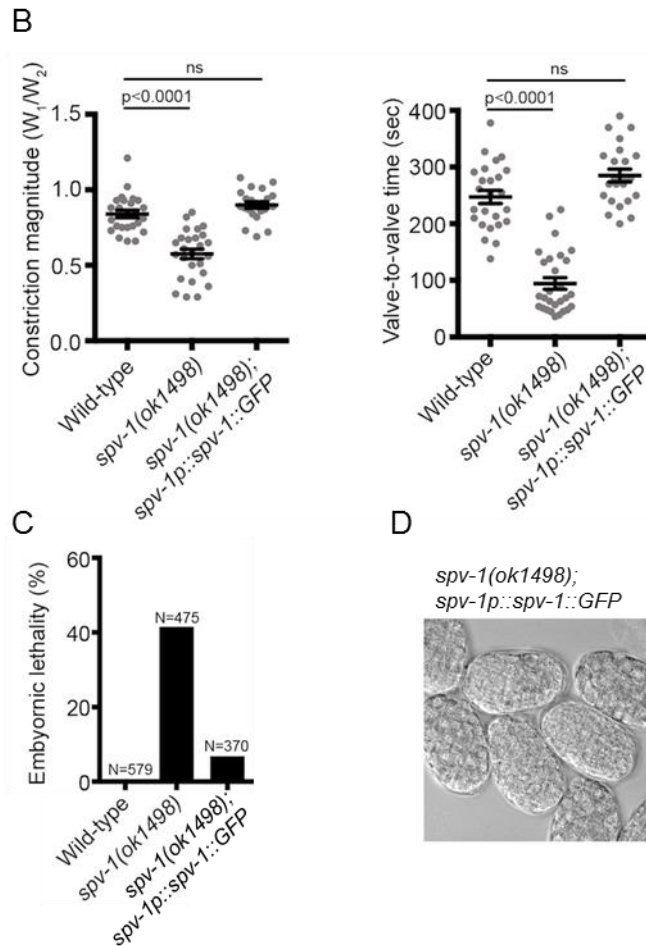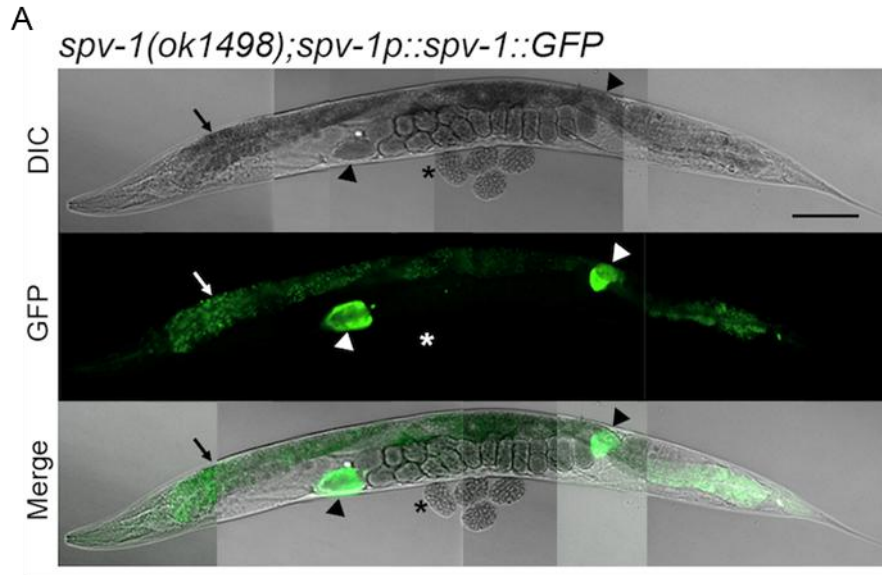
Figure 13: SPV-1 is exclusively expressed in the spermatheca.

(A) SPV-1::GFP under the regulation of its endogenous promoter is expressed in the spermatheca (arrowheads). Arrows indicate autofluorescence of the gut granules. Asterisk denotes the embryos. Scale bar = 100 μm.

(B) Quantification of the constriction magnitude and valve-to-valve time in SPV-1::GFP transgenic line. Data from wild-type and *spv-1 (ok1498)* were duplicated from Figure 9. Each data point (grey dot) is a single embryo transit event. Data are represented by mean ± SEM with n ≥ 23 for each worm strain analyzed. Statistical comparisons were performed using one-way ANOVA-Tukey's multiple comparisons test.

(C) Quantification of embryonic lethality in wild-type, *spv-1 (ok1498)* and *spv-1p::spv-1::GFP* worms. Data from wild-type and *spv-1 (ok1498)* were duplicated from Figure 11. N represents the number of embryos scored.

(D) DIC image of *spv-1p::spv-1::GFP* embryos. Scale bar = 20 μm.

Reproduced with permission from Tan and Zaidel-Bar (2015).

3.2.4. SPV-1 function in the spermatheca is essential for embryogenesis

The observation of a bias in developmental arrest in round embryos (Figure 12B) combined with the lack of embryonic expression for SPV-1 (Figure 13A) suggested that the embryonic lethality associated with loss of *spv-1* function is solely contributed by the aberrant embryo morphology as a consequence of spermathecal overconstriction. To further validate that SPV-1 is not essential for embryogenesis, we drove SPV-1::GFP expression with the spermatheca specific promoter *sth-1* (Bando et al., 2005). The spermathecal specific expression of SPV-1::GFP was able to successfully rescue embryonic lethaility (Figure 14A) along with embryo shape defect (Figure 14B). Furthermore, we performed a genetic cross between *spv-1 (ok1498)* hermaphrodites with either wild-type or *spv1 (ok1498)* males and scored for embryonic lethality. If *spv-1* gene function within embryos is essential for embryonic development, the introduction of a wild-type copy of the *spv-1* locus to the *spv-1 (ok1498)* mutant should rescue the embryonic lethality of F1 heterozygous progenies but will not alleviate spermathecal overconstriction in the parent *spv-1 (ok1498)* hermaphrodite. Interestingly, we observed a slight reduction in embryonic lethality in cross-progeny regardless of the phenotype of the males (Figure 14C), probably due to the presence of an unknown relaxing effect of the male sperm on the spermatheca. Taken together, our results suggest that SPV-1 function within the spermatheca, but not within the embryo, is essential for embryogenesis. We hypothesize that embryonic lethality observed with loss of SPV-1 could be due to the irregular embryo shape as a consequence of spermathecal overconstriction.
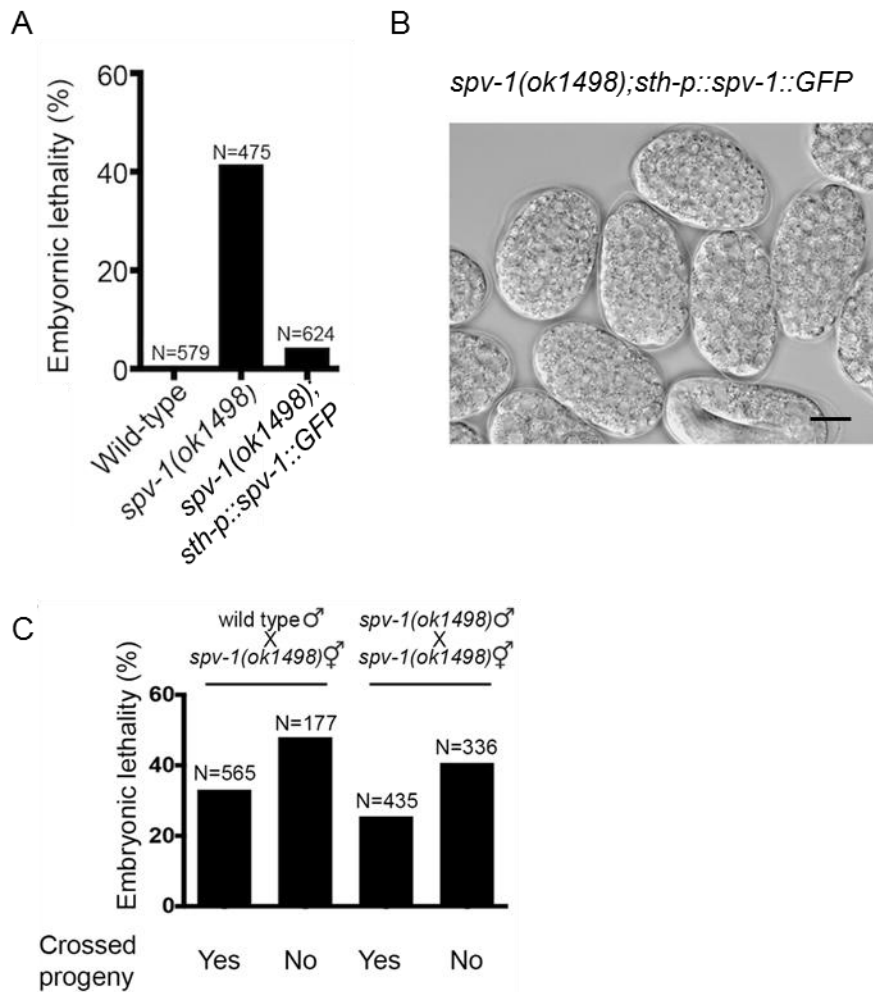
Figure 14: SPV-1 is not essential for embryo development.

(A) Quantification of embryonic lethality in wild-type, *spv-1 (ok1498)* and *sth-1p::spv-1::GFP* worms. Data from wild-type and *spv-1 (ok1498)* were duplicated from Figure 11. N represents the number of embryos scored.
(B) DIC image of *sth-1p::spv-1::GFP* embryos. Scale bar = 20 μm.
(C) Results of 3 independent mating experiments, in which embryonic lethality was quantified for self progeny and cross progeny of *spv-1(ok1498)* hermaphrodites mated with either wild-type males or *spv-1(ok1498)* males. Cross progeny was identified by the presence of males in the F1 generation.

Reproduced with permission from Tan and Zaidel-Bar (2015).

3.2.5. The RhoGAP domain of SPV-1 functions upstream of RHO-1/LET-502 signaling pathway

Since SPV-1 is a RhoGAP domain-containing protein, we hypothesized that it is regulating spermatheca contractility upstream of RHO-1/RhoA. To test this, we performed a *rho-1* knockdown by RNAi feeding in the background of *spv1- (ok1498)* mutant and tested for a phenotypic rescue in spermathecal constriction. As expected, the 24 h *rho-1* RNAi treatment successfully restored normal embryo transit (Figure 15A,B), suggesting that the hypercontractile phenotype in *spv-1* loss-of-function was due to excessive RHO-1 activity. To monitor RHO-1 levels in the spermatheca during embryo transit, we utilized a rho-biosensor harboring the rho-binding domain of *C. elegans* anillin (AHPH::GFP) (Tse et al., 2012) and drove its expression in the spermatheca with the *sth-1* promoter. The rho-binding domain of anillin selectively binds the GTP-bound form of active RHO-1, resulting in an accumulation of AHPH::GFP at the site where active RHO-1 is present, hence an increase in fluorescence intensity. In wild-type animals, we observed a gradual increase in the intensity of the RHO-1 sensor at the distal end of the spermatheca after completion of oocyte entry, and the intensity peaked during embryo exit (Figure 16A,B, arrows). In contrast, the spermatheca in *spv-1 (ok1498)* worms displayed a sharp increase in the intensity of the Rho-biosensor at the distal end of the spermatheca immediately upon completion of oocyte entry (Figure 16A,B, arrowheads). We confirmed the efficacy of the Rho-sensor by reducing RHO-1 in *spv-1 (ok1498)* through RNAi feeding. Under these conditions, the premature accumulation of the rho-biosensor in the *spv-1 (ok1498)* spermatheca was abolished (Figure 16C,D). Based on these results we concluded that in the absence of *spv-1* higher levels of activated RHO-1 lead to overconstriction of the spermatheca.

We postulated that the RhoGAP domain of SPV-1 is a direct upstream negative regulator of RHO-1 activity. To test this, we performed an in vitro RhoGAP activity assay using purified proteins. Incubating recombinant mammalian RhoA protein with the RhoGAP domain of SPV-1 in the presence of GTP showed a significant increase in phosphate released ($p<0.001$) as compared to the intrinsic hydrolysis of RhoA with GTP alone (Figure 17A). To establish that the RhoGAP domain is functionally essential in vivo, we engineered a construct with a nonfunctional RhoGAP domain, SPV-1(R635K)::GFP, by introducing a point mutation at the RHO-1 catalytic site. As expected, the deadGAP construct failed to rescue the overconstriction phenotype of *spv-1 (ok1498)* in terms of constriction magnitude and valve-to-valve time (Figure 17B). We obtained similar results with a complete deletion of the RhoGAP domain (Figure 17B). These findings corroborate our hypothesis that the RhoGAP domain of SPV-1 functions to suppress RHO-1 activity in the spermatheca.

It is well established that RhoA regulates contractility via two distinct pathways: 1) by promoting actin polymerization through activation of diaphanous formins (Watanabe et al., 1999) and 2) activation of Rho-kinase and subsequence phosphorylation of myosin light chain (Amano et al., 1996; Kimura et al., 1996). To test if the first mechanism was at play in the spermatheca, we utilized YFP::ACT-5 as an actin marker to visualize actin organization in the spermatheca. There were no discernable differences between circumferential actin bundles in wild-type and *spv-1 (ok1498)* mutant worms at the resolution of the light microscope (Figure 18A). To determine the contribution of LET-502/Rho kinase in RHO-1-dependent spermathecal constriction, we performed a genetic cross between *spv-1 (ok1498)* and the *let-502*

(sb106) hypomorphic mutant. The *spv-1(ok1498);let-502(sb106)* double mutant restored the constriction magnitude to a similar ratio to the *let-502 (sb106)* single mutant alone (Figure 18B). This is in line with the hypothesis that SPV-1 negatively regulates contractility upstream of RHO-1/LET-502. However, the slight increase in valve-to-valve time for the *spv-1 (ok1498);let-502 (sb106)* double mutant was not significantly different from *spv-1 (ok1498)* mutant alone (Figure 18B). One plausible explanation for the incomplete rescue could be that the hypomorphic properties of *let-502 (sb106)* allele were not sufficient to fully alleviate the overconstriction phenotype.
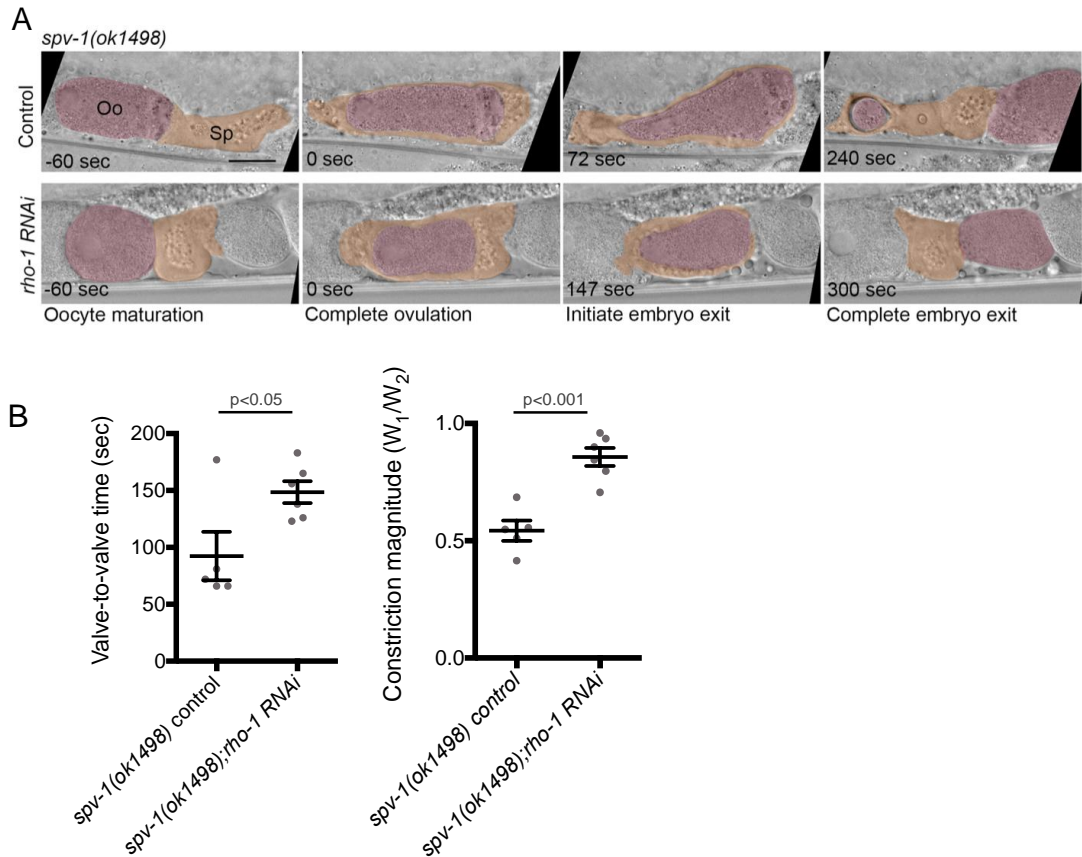
Figure 15: Reduced RHO-1 activity alleviates the *spv-1(ok1498)* mutant phenotype.

(A) Representative images of embryo transit events in *spv-1 (ok1498)* mutants treated with control (L4440) or *rho-1 (RNAi)*. Complete ovulation is referred to as time 0 sec. The precocious and hyperconstricted phenotype of the mutant spermatheca is reverted to wild-type phenotype under *rho-1(RNAi)* condition. Oo: oocyte, Sp: spermatheca. Scale bar = 20 μm.
(B) Quantifications of valve-to-valve time and constriction magnitude *spv-1 (ok1498)* mutant animals treated with control (L4440) or *rho-1 (RNAi)*. Each data point (grey dot) is a single embryo transit event. Data are represented by mean ± SEM with n ≥ 5 for each worm strain analyzed. Statistical comparisons were performed using two-tailed unpaired t test.

Figure 15A is reproduced with permission from Tan and Zaidel-Bar (2015).
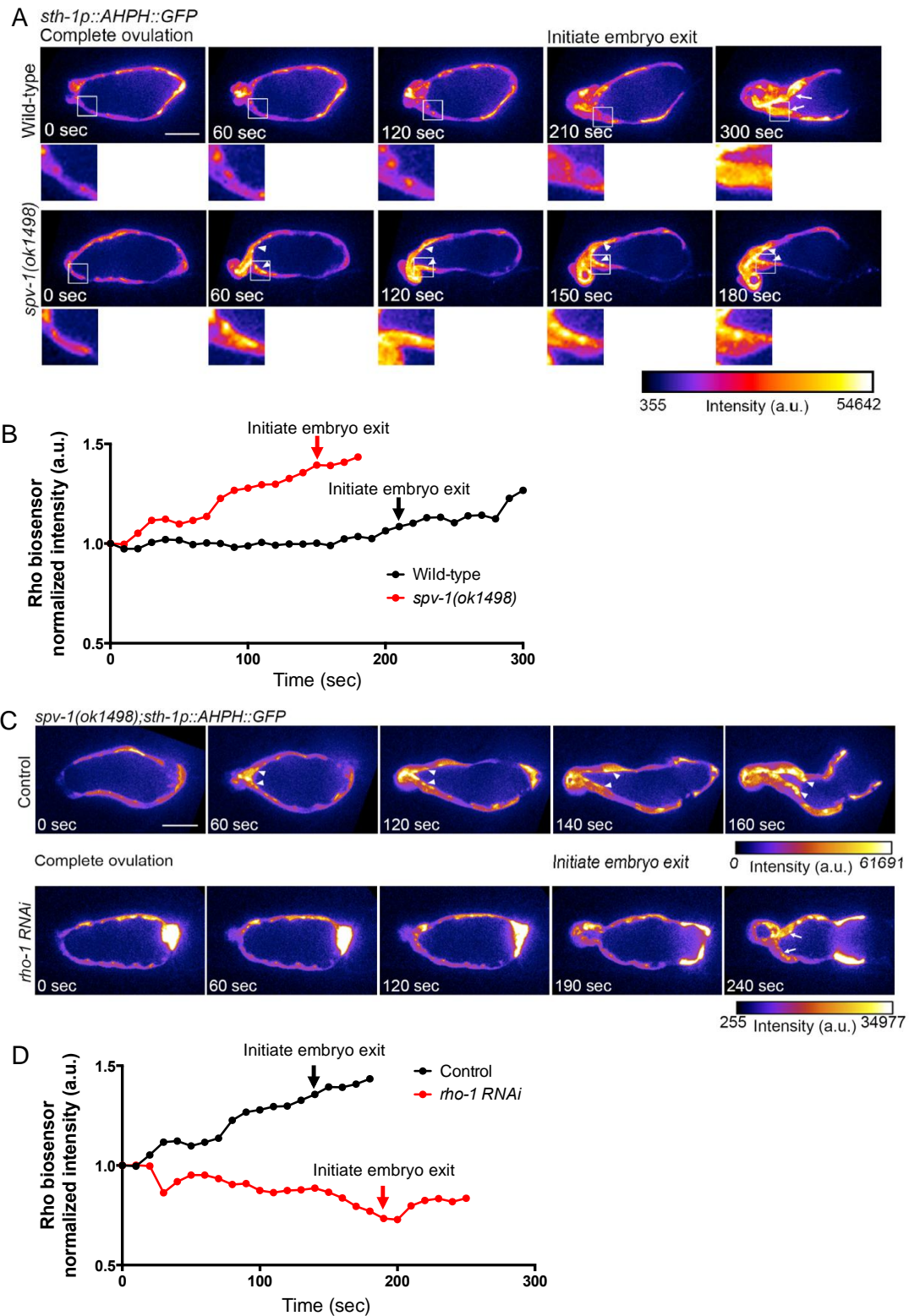
Figure 16: RHO-1 activity is elevated in *spv-1 (ok1498)* mutant.

(A) Representative images of wild-type and spv-1 (ok1498) mutant worms carrying the active RHO-1 biosensor (AHPH::GFP). Arrows and arrowheads indicate an accumulation of AHPH::GFP. Scale bar = 20 μm.

(B) Line plots of mean fluorescence intensity measured at 10 sec intervals for the ovulation process shown in (A). Arrows mark the point when embryo exit begins. The

end of the line corresponds with the final image at 300 sec and 180 sec for wild-type and *spv-1 (ok1498)* mutant respectively.

(C) Live imaging of active RHO-1 biosensor (AHPH::GFP) in *spv-1(ok1498)* spermatheca in control (L4440) and *rho-1(RNAi)* conditions to demonstrate the efficacy of the Rho-biosensor. Arrows and arrowheads indicate an accumulation of AHPH::GFP. Scale bar = 20 μm.

(D) (B) Line plots of mean fluorescence intensity measured at 10 sec intervals for the ovulation process shown in (C). Arrows mark the point when embryo exit begins. The end of the line corresponds with the final image at 160 sec and 240 sec for control and *rho-1 RNAi*-treated worms respectively.
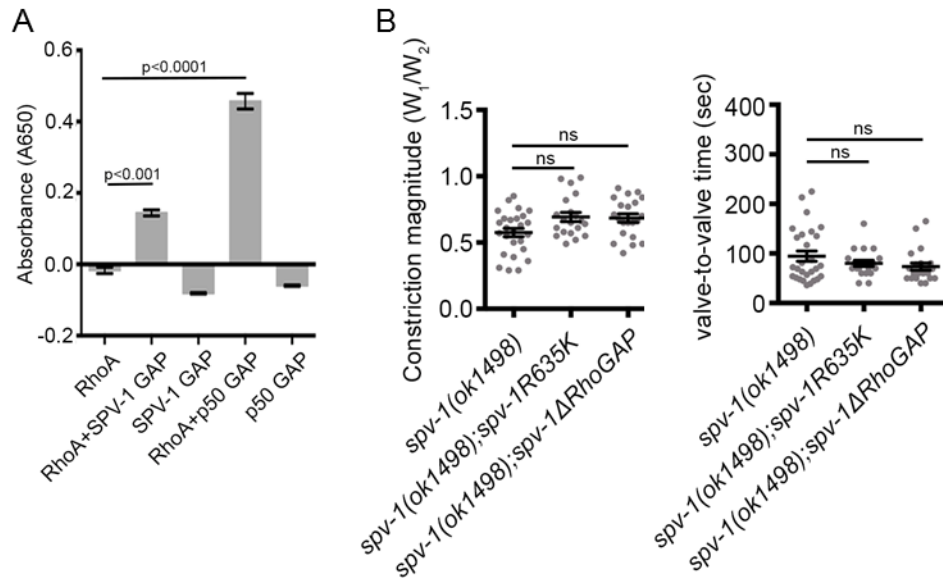
Figure 17: The RhoGAP domain of SPV-1 negatively regulates RHO-1 activity.

(A) In vitro RhoGAP activity assay measuring GAP activity toward recombinant mammalian RhoA shows GAP activity of the RhoGAP domain of SPV-1. The catalytic domain of human p50 GAP was used as a positive control.

(B) Quantification of the constriction magnitude and valve-to-valve time in *spv-1 (ok1498)* and transgenic worms depleted of RhoGAP activity. Data from *spv-1 (ok1498)* is duplicated from Figure 9. Each data point (grey dot) is a single embryo transit event. Data are represented by mean ± SEM with n ≥ 23 for each worm strain analyzed. Statistical comparisons were performed using one-way ANOVA-Tukey's multiple comparisons test.

Reproduced with permission from Tan and Zaidel-Bar (2015).
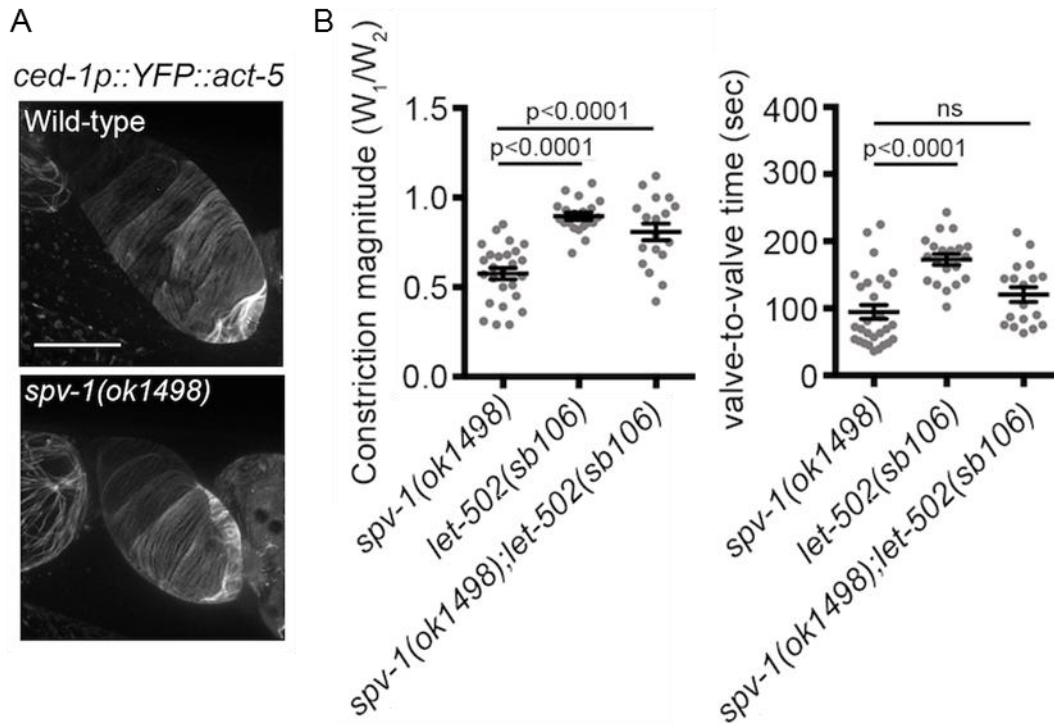
Figure 18: LET-501/Rho-kinase functions downstream of SPV-1.

(A) Circumferential actin bundles in wild-type and *spv-1 (ok1498)* visualized with YFP::ACT-5. Image from the wild-type panel is duplicated from Figure 6.
(B) Quantification of the constriction magnitude and valve-to-valve time in *spv-1 (ok1498)* and *let-502 (sb106)* single and double mutants. Data from *spv-1 (ok1498)* is duplicated from Figure 9. Each data point (grey dot) is a single embryo transit event. Data are represented by mean ± SEM with n ≥ 23 for each worm strain analyzed. Statistical comparisons were performed using one-way ANOVA-Tukey's multiple comparisons test.

Reproduced with permission from Tan and Zaidel-Bar (2015).

3.2.6. SPV-1 localizes transiently to the plasma membrane

To investigate the intracellular localization of SPV-1 during an embryo transit event, we performed time-lapse imaging of SPV-1::GFP transgenic worms using confocal microscopy (Figure 19A). During the initial phase of embryo transit (Figure 19A, time 0 sec), an intense accumulation of SPV-1::GFP was observed at the apical membrane. A line profile taken across the width of a single spermatheca cell at 0 sec gave a distinct peak (Figure 19A, black triangle) representing enrichment of SPV-1::GFP at the membrane compared to the intensity at the cytoplasm (Figure 17A, open triangle). Interestingly, membrane accumulation of SPV-1::GFP was gradually diminished and disappeared (180 sec) prior to opening of the sp-ut valve (360 sec) (Figure 19A). We attributed the gradual detachment of SPV-1 from the membrane to the flattening of nanoscopic membrane folds in the apical membrane of spermathecal cells.

To correlate the spatiotemporal changes of SPV-1 membrane localization with RHO-1 activity, we quantified the membrane-to-cytoplasm ratio of SPV-1 alongside quantification of RHO-1 levels from completion of ovulation to the end of embryo transit (Figure 19B). We observed a gradual reduction in membrane localization of SPV-1::GFP during the course of embryo transit and membrane signal was completely lost halfway through the embryo retention period. At the same time, total Rho-biosensor intensity displayed the opposite trend with lower levels in the initial stage of embryo transit that reached maximum intensity just prior to completion of embryo exit. The complementary trend of SPV-1 localization and RHO-1 activation led us to speculate that membrane-localized SPV-1 functions to suppress RHO-1

activity. Gradual detachment of SPV-1 from the membrane during embryo transit allowed RHO-1 levels to increase and thus initiate constriction.
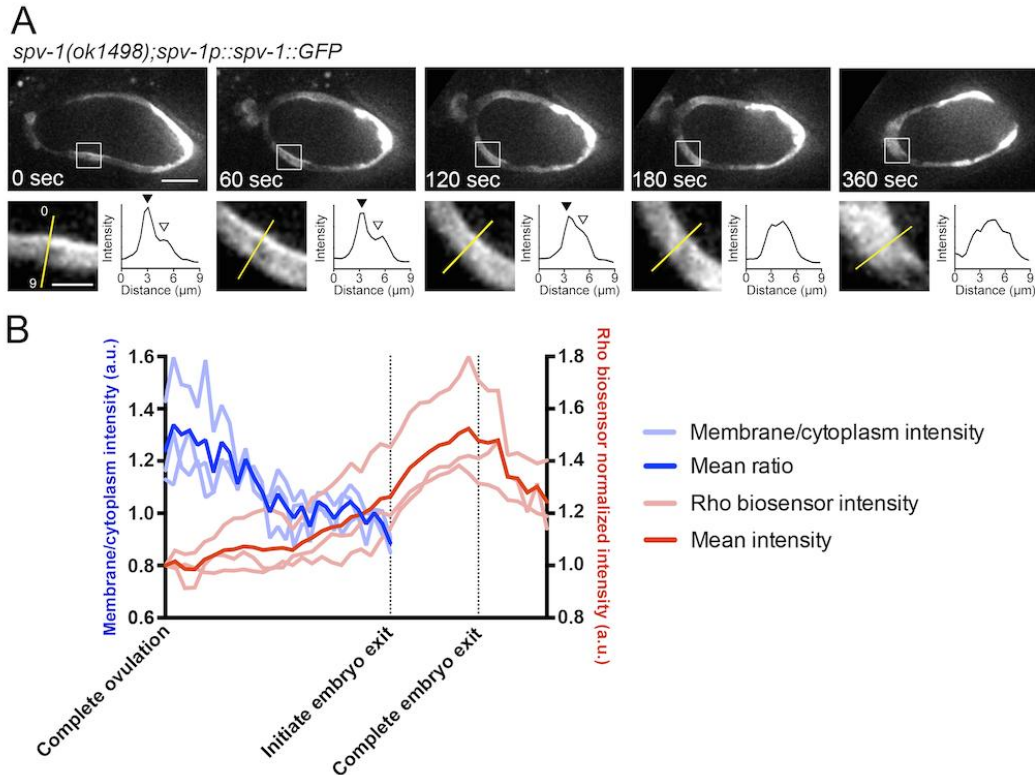
Figure 19: SPV-1 is transiently localized to the apical plasma membrane.

(A) Representative images of SPV-1::GFP driven by the *spv-1* promoter showing its subcellular localization during embryo transit. Graphs show the intensity profile of lines drawn perpendicular to the spermatheca cells. Black arrowhead indicates the peak intensity corresponding to the apical membrane. Open arrowhead represent the baseline intensity in the cytoplasm. Scale bar: whole spermatheca – 20 μm; inset – 5 μm.

(B) Quantification of SPV-1::GFP membrane accumulation and AHPH::GFP total intensity during embryo transit. The valve-to-valve time (time interval between completion of ovulation and initiation of embryo exit) on the x axis is normalized to a scale of 0–1 to enable the line plots to be superimposed on the same graph. Light-colored lines represent individual embryo transit events; bold lines are mean values quantified from the light-colored lines.

Reproduced with permission from Tan and Zaidel-Bar (2015).

3.2.7. SPV-1 contains a novel F-BAR domain

Next, we sought to understand how transient SPV-1 localization is regulated. To this end we first performed a bioinformatics analysis on the SPV-1 amino acid sequence to elucidate the protein domain architecture. A conserved domain search (Marchler-Bauer et al., 2011) revealed that in addition to the RhoGAP domain, SPV-1 also contains an N terminus Fes/Cip4 homology (FCH) domain and a phorbolesters/diacylglycerol binding (C1) domain (Figure 20A, top panel). A coiled-coil motif prediction software (McDonnell et al., 2006) predicted (with probability score > 0.5) the presence of a coiled-coil (CC) region closely succeeding the FCH domain (Figure 20A, top panel). Based on previous studies, an FCH followed by a coiled-coil domain could indicate the presence of an F-BAR domain (Itoh et al., 2005; Tsujita et al., 2006). Figure 20B, bottom panel shows the predicted protein structure of full-length SPV-1 modeled using Phyre2 with 78% of residues modeled at >90% confidence (Kelley and Sternberg, 2009).

To investigate the conservation of the putative F-BAR domain across species, we first identified orthologs of SPV-1 from sponges to mammals using the Domain Enhanced Lookup Time Accelerated Basic Local Alignment Search Tool (DELTA-BLAST) (Boratyn et al., 2012). Noteworthy, vertebrates have three SPV-1 orthologs while metazoan species up to chordates only have a single ortholog. The three SPV-1 human orthologs are: Rho GTPase-activating protein 29 (ARHGAP 29/PARG1), GEM interacting protein (GMIP) and human minor histocompatibility antigen 1 (HMHA1). It is noteworthy that a reciprocal BLAST of the putative orthologs also identified SPV-1 as the closest relative in *C. elegans*, We performed a conserved domain search and identified that the human orthologs share the same domain

architecture as SPV-1. A single study has reported HMHA1 to harbor a BAR domain (de Kreuk et al., 2013) while PARG1 and GMIP have yet to be characterized. Next, we performed a sequence alignment of the F-BAR domain with the closest ortholog of selected organisms at various milestones of the evolutionary tree, and found a high degree of conservation of the F-BAR between SPV-1 orthologs of distinct species (Figure 20B). To further understand which subfamily of F-BAR domain is SPV-1 associated with, we performed a phylogenic analysis of the F-BAR domain of SPV-1 and its human orthologs along with all known F-BAR domains in *C. elegans* and human. As expected, F-BAR domains from the various subfamilies formed individual clusters (Figure 20C). Interestingly, the F-BAR domain of SPV-1 and its orthologs formed a distinct cluster (Figure 20C), indicating that we discovered a novel subfamily of F-BAR domains.

F-BAR domains form homodimers with a characteristic concave-shaped protein structure. To identify if the F-BAR domain of SPV-1 takes on this characteristic appearance, we modeled the F-BAR domain with I-TASSER (Roy et al., 2010) using the 2.4 Å N-terminal crystal structure of GMIP (PDB ID:3QWE) as a template. The predicted model has a confidence score of -0.96 (in a scale of -5 to 2) Figure 20D (top panel) shows a side view of the predicted SPV-1 F-BAR domain in dimer form. The dimer displays a shallow concave curvature as expected for F-BAR domains. The bottom panel, showing the membrane-interacting surface, highlights the clustering of positively charged amino acid residues (indicated in blue) reminiscent to the characteristics of F-BAR domains. The aggregation of positive charges facilitates binding to the negatively charged plasma membrane.
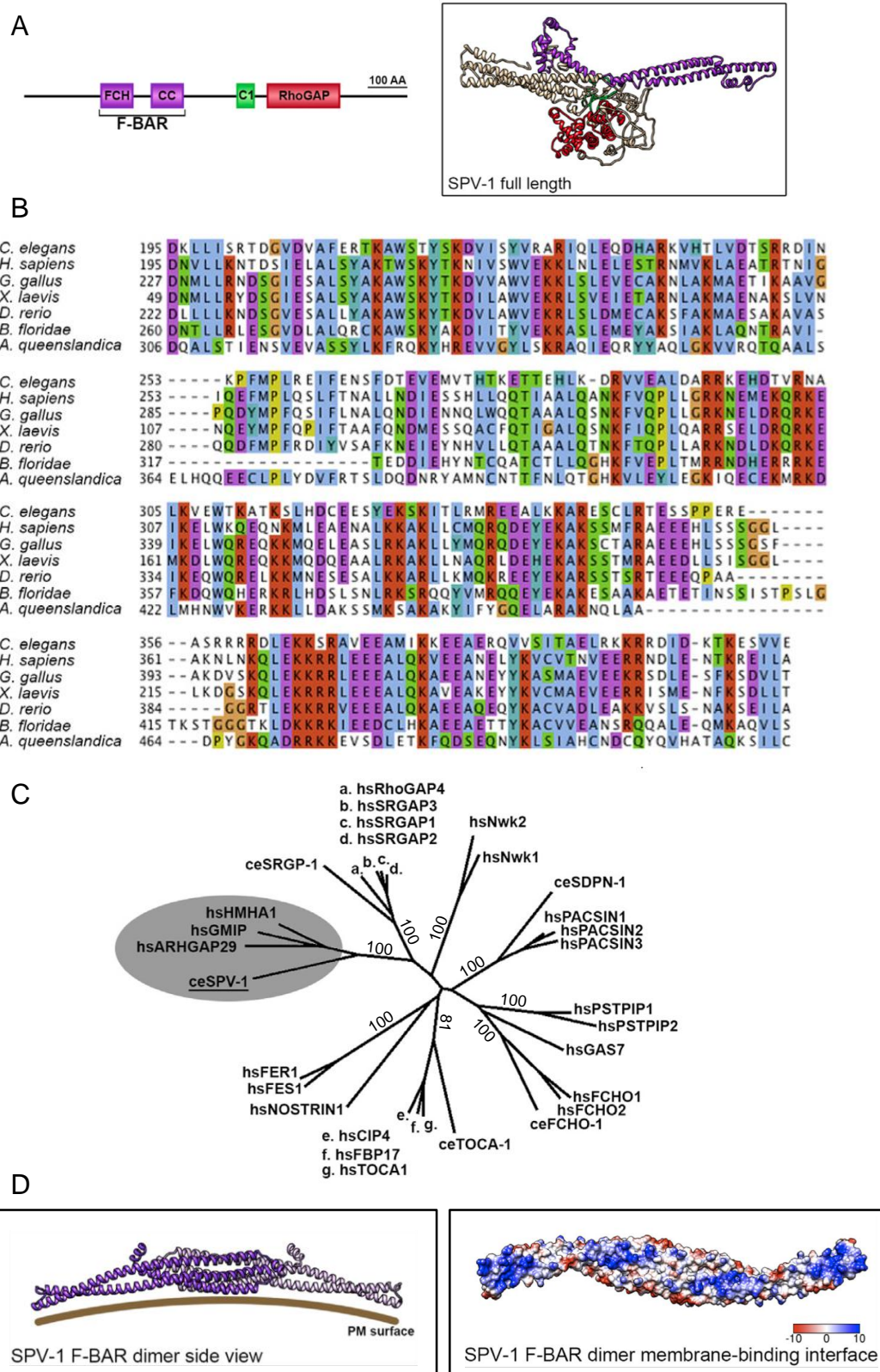
Figure 20: Bioinformatics analysis of SPV-1.

(A) Left panel: Protein domain architecture of SPV-1. Right panel: Structure prediction of full-length SPV-1. Purple: F-BAR domain, Green: C1 domain, Red: RhoGAP domain.

(B) Multiple sequence alignment of the F-BAR domains from a selection of SPV-1 orthologs. Blue, A, I, L, M, F, W, V, and C; red, R and K; green. N, Q, S, and T; pink, C; magenta, E and D; orange, G; cyan, H and Y; yellow, P. Refer to http://www.jalview.org/help/html/colourSchemes/clustal.html for the full color scheme.

(C) Unrooted phylogenic tree depicting human F-BAR domains and selected *C. elegans* orthologs. The F-BAR domain of SPV-1 and its human orthologs (HMHA1, GMIP, and ARHGAP29) form a distinct group (gray cloud). Significance of each cluster is calcutaed by bootstrap analysis where 100 represents maximal suport. ce, *C. elegans*; hs, H. sapiens.

(D) Left panel: Ribbon side view of a predicted dimer structure of the F-BAR domain of SPV-1. The predicted structure adopts a shallow concave curve. Right panel: The membrane-interacting surface is punctuated with positive amino acid residues highlighted in blue and negative residues in red.

Reproduced with permission from Tan and Zaidel-Bar (2015).

3.2.8. F-BAR domain of SPV-1 is essential for membrane localization

To experimentally determine the contribution of the F-BAR domain for SPV-1 membrane localization, we engineered a deletion of the predicted F-BAR domain (AA 195 to 405) from the *spv-1::GFP* construct. As expected, no membrane accumulation was observed throughout the course of embryo transit in *spv-1 (ok1498)* mutant worms expressing SPV-1ΔF-BAR::GFP (Figure 21A). In a line profile of across a spermathecal cell width, no distinct peak was observed, contrary to those from Figure 19A. However, we were unable to obtain transgenic strains with an expression level that is comparable to other variants of the *spv-1::GFP* constructs. Absence of membrane localization could be an artifact of low expression levels. A possible reason for the low expression could be due to loss of regulatory elements within the introns that were removed with the truncation of the F-BAR sequence. To circumvent this problem, we replaced the *spv-1* promoter with another spermatheca-specific promoter, *sth-1*. Even with higher expression, we still did not observe any enrichment of SPV-1ΔF-BAR::GFP on the apical membrane throughout the course of embryo transit (Figure 21B). This indicates that the F-BAR region is essential for the transient translocation of SPV-1 to the membrane.

Interestingly, loss of the F-BAR domain did not hinder the ability of SPV-1 to rescue the mutant phenotype in terms of constriction magnitude but prolonged the valve-to-valve time. The ratio between the distal and proximal width of the spermatheca between wild-type, *spv-1 (ok1498);spv-1p::SPV-1* and *spv-1 (ok1498);sth-1p::SPV-1ΔF-BAR* worms were not significantly different (Figure 21C). Valve-to-valve time in the worms carrying the *spv-1 (ok1498);sth-1p::SPV-1ΔF-BAR* array was slightly but significantly elevated compared to wild-type control ($p<0.01$, $n = 26$). We attributed

the increased valve-to-valve time to over-activation of the RhoGAP activity. Besides serving to target SPV-1 the membrane, the F-BAR domain could also act as an auto-inhibitory signal to prevent excessive RhoGAP activity when SPV-1 is cytoplasmic. Hence, loss of the F-BAR domain would result in enhanced RhoGAP activity. Indeed, the auto-inhibition between an F-BAR and RhoGAP domain has been reported in *C. elegans* SRGP-1 and also human HMHA-1, one of the human orthologs of SPV-1 (de Kreuk et al., 2013; Zaidel-Bar et al., 2010). Unfortunately, our attempt to perform a pulldown assay using bacterially synthesized F-BAR and RhoGAP fragments of SPV-1 to test for direct interaction was unsuccessful. It will be interesting to further investigate if an auto-inhibition between the F-BAR and RhoGAP domain of SPV-1 is caused by steric hindrance instead.
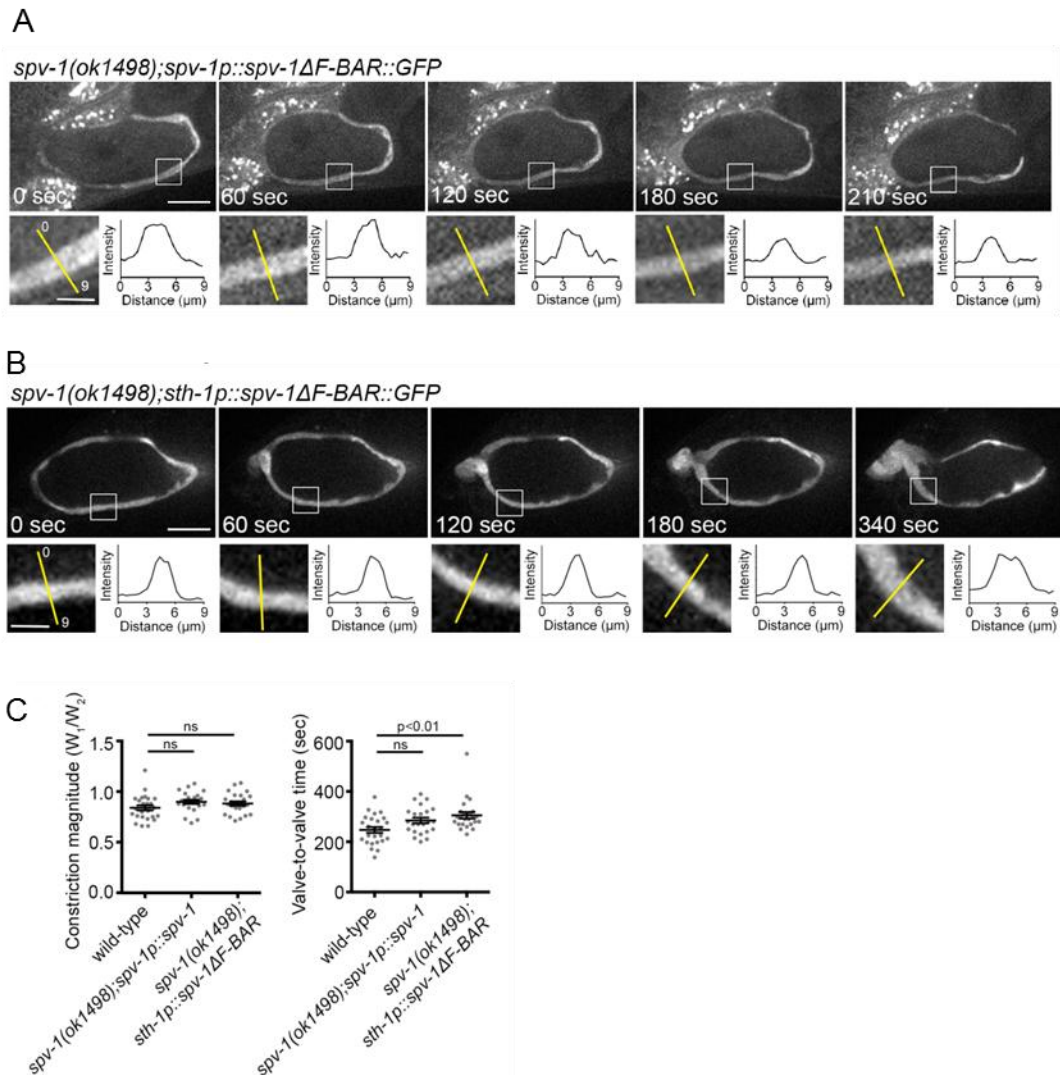
Figure 21: The F-BAR domain of SPV-1 is essential for membrane localization.

(A) Representative images of SPV-1ΔF-BAR::GFP driven by the *spv-1* promoter showing its subcellular localization during embryo transit. Graphs show the intensity profile of lines drawn perpendicular to the spermatheca cells. Scale bar: whole spermatheca – 20 μm; inset – 5 μm.
(B) Similar to (A) except for the change to the *sth-1* promoter.
(C) Quantification of the constriction magnitude and valve-to-valve time in SPV-1::GFP transgenic lines. Data from wild-type and *spv-1(ok1498)::spv-1p::SPV-1* were duplicated from Figure 9 and Figure 12. Each data point (grey dot) is a single embryo transit event. Data are represented by mean ± SEM with n ≥ 23 for each worm strain analyzed. Statistical comparisons were performed using one-way ANOVA-Tukey's multiple comparisons test.

Reproduced with permission from Tan and Zaidel-Bar (2015).

3.2.9. The F-BAR domain of SPV-1 is recruited to the membrane upon trypsinization of HeLa cells

To directly test the idea of the F-BAR domain of SPV-1 can respond to changes in membrane topology, we expressed F-BAR::GFP in HeLa cells. We used trypsin to stimulate HeLa cell detachment from the membrane and rounding up. A similar treatment in CHO cells resulted in formation of nano-membrane curvature upon trypsin treatment (Kapustina et al., 2013). In isotonic buffer, F-BAR::GFP was observed to be cytoplasmic (Figure 22). Upon trypsinization and rounding of the cells, F-BAR::GFP was seen to gradually accumulate at the plasma membrane. The plasma membrane visualized with the membrane dye DiI 561 was largely homogenous throughout the trypsin treatment, thus ruling out the possibility that the increase in F-BAR::GFP intensity was due to the increase in membrane per unit area. Our result implies that the F-BAR domain of SPV-1 is recruited to the region of convoluted membrane produced during cell detachment from the substrate, further consolidating the fact that the F-BAR domain of SPV-1 acts as a mechanical sensor of membrane topology to regulate the intracellular localization of SPV-1 during embryo transit.
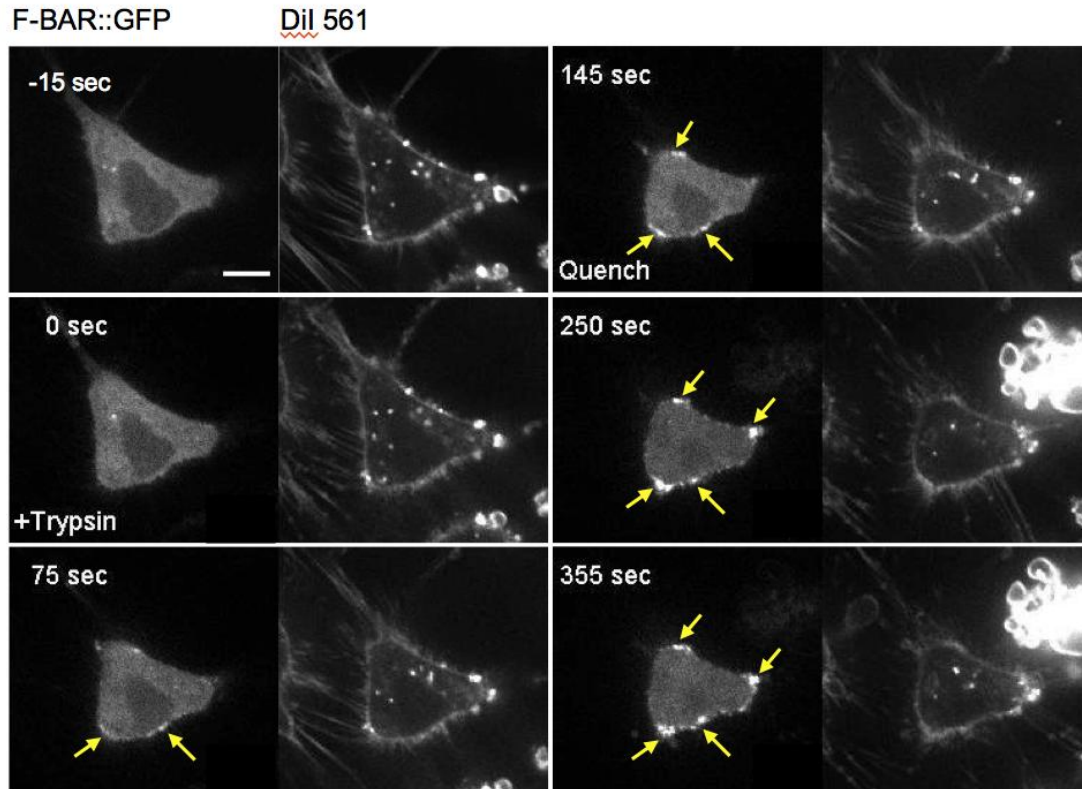
Figure 22: F-BAR::GFP accumulates at the plasma membrane of upon trypsin treatment of HeLa cell.

Images show the accumulation of F-BAR::GFP at the cell membrane (yellow arrows) 75 sec after the addition of Trypsin. The reaction was quenched at 145 sec by washing out Trypsin to prevent complete dissociation of the cell from the surface. The plasma membrane was visualized with DiI 561 membrane dye. Scale bar=20 μm.

3.2.10. <u>Spatial control of SPV-1 localization is essential for initiation of contractility</u>

The evidence thus far suggested that during embryo transit, stretching of the spermathecal cells is sensed by the F-BAR domain, leading to detachment of SPV-1 from the membrane and subsequently increase in RHO-1 activity to initiate constriction. To directly test the importance of SPV-1 localization in regulating spermathecal constriction, we generated a chimeric SPV-1 ΔF-BAR (PH)::GFP in which the F-BAR domain was replaced by a plekstrin homology (PH) domain from rat phospholipase C gamma 1 (PLCδ1). Mutant transgenic worms carrying the chimeric SPV-1 construct displayed permanent SPV-1::GFP localization on the apical membrane (Figure 23A, top and middle panel). Phenotypically, the chimeric worms had spermathecae with multiple trapped embryos (Figure 23A bottom panel, and Figure 23B). Instead of a single embryo transiting through the spermathecal in approximately 6 min, the constitutive membrane-bound SPV-1 spermatheca failed to constrict and none of the multiple embryos exited the spermatheca during the 30 min imaging period. We postulate the permanent docking of the RhoGAP domain of SPV-1 at the membrane resulted in constant suppression of RHO-1 activity and thus reduced spermathecal constriction, which manifested in trapped embryos. This suggests that the detachment of SPV-1 from the membrane functions to initiate spermathecal contractility and embryo exit.
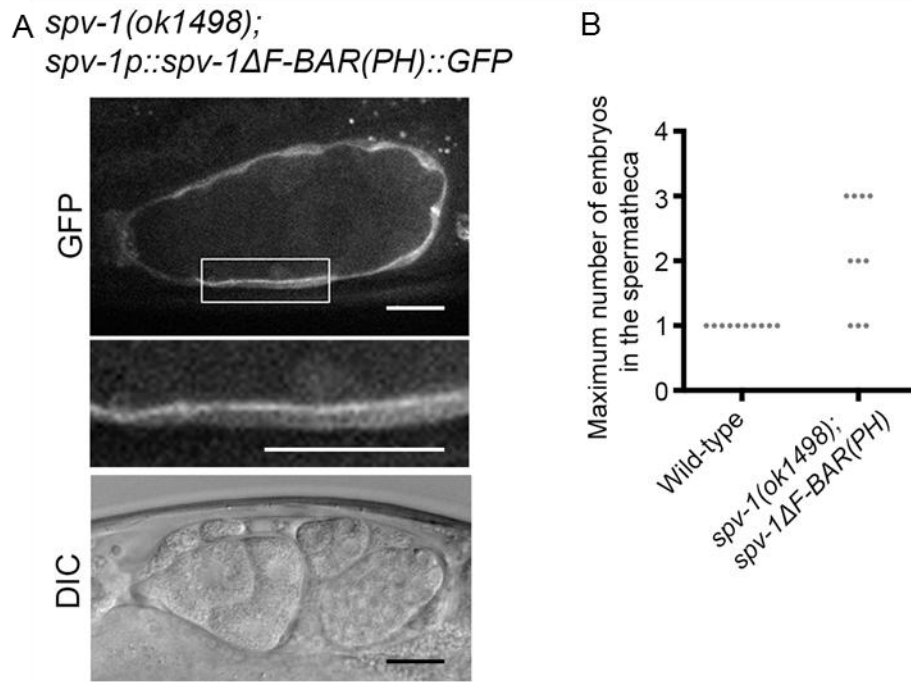
Figure 23: Transient localization of SPV-1 is essential for embryo exit.

(A) Representative image of the localization of chimeric SPV-1::GFP. The F-BAR domain of SPV-1 was replaced with a PH domain. Top panel indicates SPV-1 GFP enrichment at the membrane. Middle panel is the inset from the cropped region. Bottom panel illustrates multiple trapped embryos in the spermatheca. Scale bar =20 μm and 10 μm for the full spermathecal and cropped region respectively.
(B) Quantification of the maximum number of embryos in the spermatheca during a 30 min imaging period. Each dot represents an independent experiment. n = 10 for each strain.

Reproduced with permission from Tan and Zaidel-Bar (2015).

3.3. Identification and characterization of a RhoGEF involved in spermathecal constriction.

3.3.1. *rhgf-1* loss-of-function rescues the *spv-1 (ok1498)* overconstriction phenotype

The regulation of Rho GTPases occurs in a cycle (Figure 2). The GTPase enhancing activity of RhoGAPs is counteracted by GDP to GTP exchange catalyzed by RhoGEFs. We sought to identify the RhoGEF(s) involved in counteracting SPV-1 in the activation of RHO-1 in the spermatheca.

Since RhoGAPs and RhoGEFs perform opposing roles in regulating RhoA activity, we hypothesized that the loss of a spermathecal-associated RhoGEF would alleviate the *spv-1 (ok1498)* mutant phenotype. To this end, we performed an RNAi knockdown screen for all 20 *C. elegans* RhoGEFs in the background of *spv-1 (ok1498)* mutant and looked for the rescue of embryo shape defect. The identity of the RhoGEFs is listed in Table 6. To score the degree of rescue, we dissected 10 worms for each gene knockdown and assessed how many of the worms had a majority of 'wild-type'-looking embryos (Table 7). Of the 20 RhoGEFs tested, loss of *rho guanine nucleotide exchange factor* (*rhgf*)-*1* successfully restored the embryo morphology for all 10 worms dissected (Table 7, red highlight). Live imaging of embryo transit events revealed a rescue of the overconstriction phenotype in *spv-1 (ok1498);rhgf-1(RNAi)* spermatheca (Figure 24, n = 4). RHGF-1 has been previously reported to function upstream of RHO-1 in the release of acetylcholine at the synapses of motor neurons (Hiley et al., 2006). We propose that in the spermatheca, loss of *rhgf-1* led to reduced RHO-1 activity thus rescuing the *spv-1 (ok1498)* hyperconstriction phenotype.

81

Table 6: List of RhoGEF-containing genes knocked down by RNAi feeding in the *spv-1 (ok1498)* **mutant background.**

Gene Name
cgef-1
cgef-2/tiam-1
ect-2
exc-5
F52D10.6
pix-1
R02F2.2
rhgf-1
rhgf-2
sos-1
tag-218/ephx-1
tag-52
tag-77
uig-1
unc-73
unc-89
vav-1
Y105E8A.24
Y37A1B.17
Y95B8A.12

Table 7: Tabulation of results for embryo shape rescue in *spv-1 (ok1498)* treated with RhoGEF RNAi feeding.

L4440 empty vector and *rho-1*-targeting RNAi feeding clones were used as negative and positive controls respective. Knockdown of *rhgf-1* (highlighted in red) shows 100% restoration of embryo shape to wild-type dimensions.

Target gene	No. of worms with 'WT'-looking embryos
L4440 (-ve control)	1/10
rho-1 (+ve control)	10/10
cgef-1	1/10
cgef-2/tiam-1	0/10
ect-2	0/10
exc-5	1/10
F52D10.6	1/10
pix-1	0/10
R02F2.2	1/10
rhgf-1	10/10
rhgf-2	1/10
sos-1	1/10
tag-218/ephx-1	0/10
tag-52	1/10
tag-77	1/10
uig-1	2/10
unc-73	7/10
unc-89	0/10
vav-1	0/10
Y105E8A.25	7/10
Y37A1B.17	0/10
Y95B8A.12	1/10
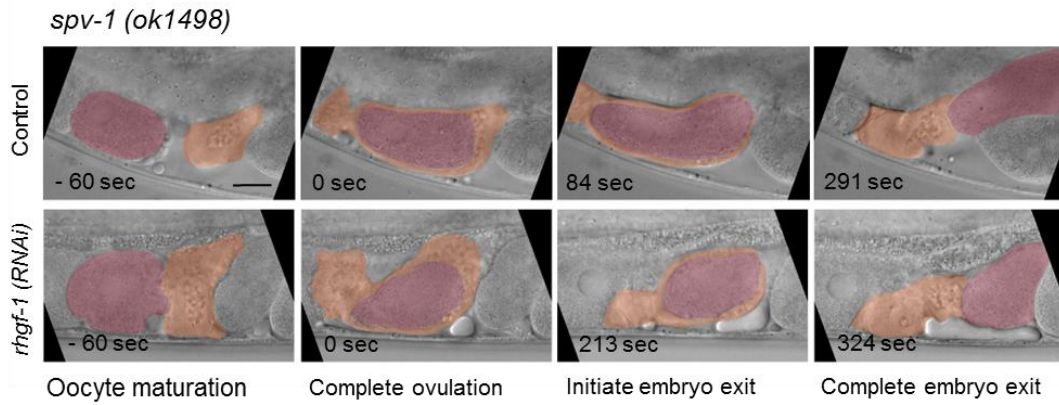
Figure 24: Loss of *rhgf-1* in the *spv-1 (ok1498)* mutant alleviates hyperconstriction in the spermatheca.

Representative images of embryo transit events in *spv-1 (ok1498)* mutants treated with L4440 empty plasmid (negative control, top panel) and *rhgf-1 (RNAi)*. Complete ovulation is referred to as time 0 sec. The precocious and hyperconstricted phenotype of the mutant spermatheca is reverted to wild-type phenotype under *rhgf-1 (RNAi)* condition. Scale bar = 20 μm.

3.3.2. *rhgf-1* loss-of-function results in trapped embryos in the spermatheca

We expected the loss of *rhgf-1* to completely abolish the contractile ability of the spermatheca since RHO-1 activation would be absent. In wild-type worms, knockdown of *rhgf-1* for 48 hours showed 60% of ovulation events with incomplete embryo exit (n = 5). The incomplete penetrance of the loss-of-function phenotype could be due to two reasons: 1) incomplete knockdown of the *rhgf-1* mRNA transcript by RNAi or 2) *rhgf-1* is not the sole activator or RHO-1 in the spermatheca.

3.3.3. RHGF-1 is expressed in the spermathecal cells

A previous study on the transcriptional activity of RhoGEFs in gonadogenesis using 2.5 kb of the *rhgf-1* promoter to drive cytoplasmic GFP reported expression in the L4 spermathecal epithelium (Ziel et al., 2009). Using the same worm strain, we investigated the transcriptional expression of *rhgf-1* in the spermatheca of young adults. We observed spermathecal expression, with strongest expression at the distal end of the spermatheca (Figure 25). This is consistent with the fact the constriction is initiated at the distal end to facilitate embryo exit.

rhgf-1p::GFP

DIC   GFP   Merge
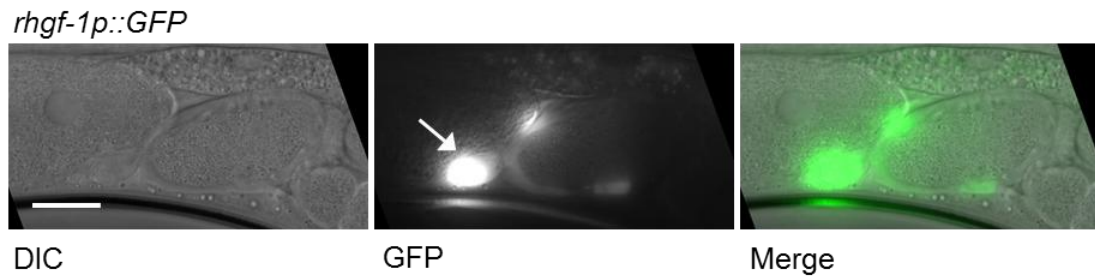
Figure 25: Transcriptional expression of RHGF-1 in the spermatheca.

GFP expression driven by the *rhgf-1* promoter is concentrated in the spermatheca, particularly at the distal end (arrow). Scale bar = 20µm.

3.4. Proposed mechanism of action

Our results suggest that RHO-1 is a key regulator of spermathecal contractility. We have identified SPV-1 (a RhoGAP domain-containing protein) and RHGF-1 (a RhoGEF domain-containing protein) as upstream regulators of RHO-1 in the spermatheca. SPV-1 and RHGF-1 function antagonistically to regulate the amount of active RHO-1 to ensure proper cycles of constriction and relaxation during embryo transit (Figure 23).

We propose that during oocyte entry, the spermathecal cells are stretched, leading to SPV-1 detachment from the apical membrane due to unfavorable conditions for F-BAR binding. Removal of SPV-1 and its RhoGAP domain from the membrane lifts the inhibition on RHO-1. Concurrently, we hypothesize that oocyte entry also triggers the activation of RHO-1 through the RhoGEF domain of RHGF-1. The reciprocal effect of SPV-1 and RHGF-1 during oocyte entry ensures the gradual rise of RHO-1 and the subsequent activation of LET-502 to initiate spermathecal constriction. We propose that upon embryo exit, the spermathecal cells collapse, leading reattachment of SPV-1 to the apical membrane and suppression of RHO-1 activity. These events together suppress RHO-1 activity, leading to a low constriction state while the spermatheca awaits the next ovulation event.
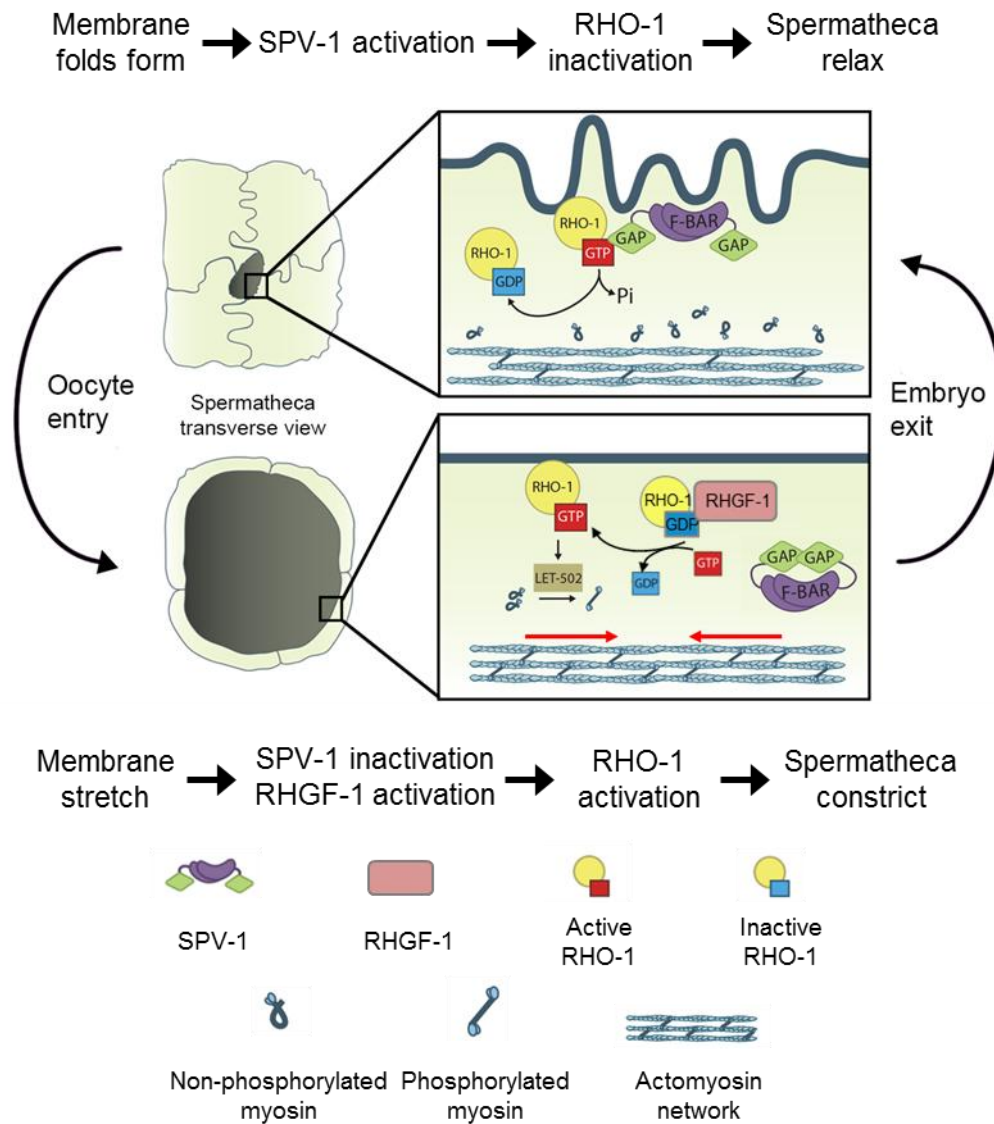
Figure 26: Model illustrating the mechanism on the regulation of spermathecal constriction by the reciprocal activity of SPV-1 and RHGF-1.

SPV-1 inactivates RHO-1 in a cyclical manner by transiently localizing to the apical membrane mediated by its F-BAR domain. When the spermatheca is collapsed, presence of membrane folds allows SPV-1 to bind to the membrane, and inactivate RHO-1 activity through its RhoGAP domain. Oocyte entry stretches the spermatheca cells and straightens out membrane folds. This leads to the detachment of SPV-1 from the membrane, thus lifting the inhibition on RHO-1 activity. Concurrently, through a yet unknown mechanism, RHO-1 is activated by RHGF-1, allowing active RHO-1 to rise beyond the threshold needed to initiate spermathecal constriction.

Adapted with permission from Tan and Zaidel-Bar (2015).

Chapter 4:

Discussion

4. Discussion

4.1. Embryo shape has profound consequences for embryonic development

In *spv-1 (ok1498)* mutants and *spv-1 (RNAi)* worms, we reported 41% and 50% embryonic lethality, respectively (Figure 11C). Based on expression data and genetic analysis, we confirmed the lack of SPV-1 function in the embryo (Figure 12A and Figure 13). This raised an interesting question regarding the cause of embryonic lethality. By plotting the embryo size against the axial ratio, we observed that embryos within the wild-type size range but with an aspect ratio below 1.49 tend to arrest prematurely while long embryos (with high aspect ratio) were largely unaffected (Figure 11B). This prompts us to hypothesize that embryo geometry is a contributing factor in determining the viability of embryos during development. A study by Minc *et. al.* revealed that geometrical constraint is an essential cue for positioning the division plane in the development of sea urchin embryos (Minc et al., 2011). One approach to test if embryonic lethality in the *spv-1 (ok1498)* mutants and *spv-1 (RNAi)* treated worms were simply due to the fact that embryos were missing some cytoplasmic content due to pinching off of the embryos or geometrical constraint is indeed contributing to embryonic development is to physically deform the embryo shape. Nghe and colleagues described the fabrication of micron-size polyacrylamide chambers for confinement of *C. elegans* larvae (Nghe et al., 2013). The advantage of using polyacrylamide in place of the more traditional polydimethylsiloxane (PDMS) is the permeability of polyacrylamide to buffered solutions to ensure proper development during long term confinement of the worms in the chambers (Nghe et al., 2013). Instead of hatched larvae, we propose to culture *C. elegans* embryos in chambers of various geometries to test the contribution of embryo shape to development. Polyacrylamide wells of round, elliptical and elongated

geometry can be used to deform and constraint embryos during development to simulate the condition observed in *spv-1 (ok1498)* and *spv-1 (RNAi)* embryos. Indeed, deformation of embryo shape using polyacrylamide wells have successfully been performed (Pierre Recouvreux, personal communication). The mechanistic relationship between geometry and embryonic development is an interesting topic for future investigation.

4.2. Human orthologs of SPV-1

DELTA-BLAST results revealed that SPV-1 has three human orthologs, namely PARG1, HMHA1 and GMIP. From bioinformatic analysis, all three human orthologs share the same domain architecture as SPV-1. Of the three orthologs, only HMHA1 has been characterized to modulate the actin cytoskeleton an cell spreading through the regulation of RhoA activity (de Kreuk et al., 2013). The same group also report the presence of a BAR domain in HMHA1 which acts as an inhibitor of the RhoGAP activity (de Kreuk et al., 2013). PARG1 is known to function as a RhoGAP protein in modulating cell shape change but the presence of an F-BAR domain has been overlooked (Saras et al., 1997). There has yet to be a published finding on the spatiotemporal localization of the SPV-1 orthologs in mammalian cells. A recent paper reported a feedback mechanism between plasma membrane tension and the activation of an F-BAR-containing protein, FBP17, regulates cell migration (Tsujita et al., 2015). FBP17 localizes to membrane invaginations at the leading edge to promote actin polymerization, while diminishing from the cell rear in response to an increase in plasma membrane tension. We hypothesize that in mammalian cells a mechanism similar to that of SPV-1 in the spermatheca could take place whereby a mammalian ortholog of SPV-1 regulates RHO-1 in a membrane curvature-dependent manner. Currently, we have an ongoing collaboration with Nils Gauthier (Mechanobiology Institute, Singapore) and his group to further elucidate the function of PARG1 during cell spreading in mouse embryonic fibroblasts (MEFs) and cell migration in mouse mammary epithelial cells (EpH4). We tested the expression levels of PARG1, HMHA1 and GMIP in both cell types by detecting the mRNA transcript levels using Reverse Transcription and semi-quantitative PCR. PARG1 was found to be expressed at the highest level in both cell types (**Figure 27**). We are currently

performing phenotypic analysis and analyzing the spatiotemporal information of full length PARG1, PARG1ΔF-BAR and PARG1ΔRhoGAP in MEFs and EpH4 cell lines during cell spreading and cell migration respectively.
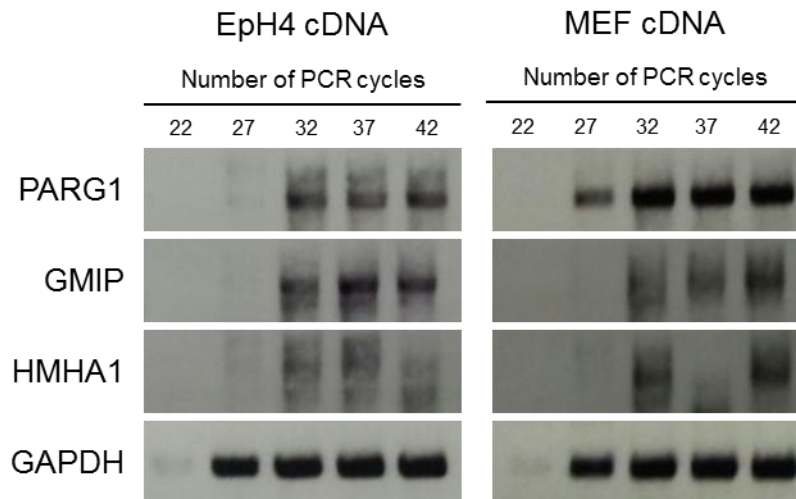
Figure 27: PARG1, GMIP and HMHA1 transcript levels in EpH4 and MEF cells.

Amplification of the PARG1 total cDNA gave distinct bands starting from cycle 32 in EpH4 cells and cycle 27 in MEF cells. GMIP transcript is only present in EpH4 cells while HMHA1 is not expressed in both cell types tested. GAPDH is used as a housekeeping control.

4.3. The F-BAR domain of SPV-1 and its orthologs form a novel subfamily

In a phylogenic analysis, we discovered that the F-BAR domains of SPV-1, along with its human orthologs, PARG1, GMIP and HMHA1, formed a distinct cluster separate from currently known human F-BAR domains (**Figure 20**C). Besides the divergence in sequences of the F-BAR domain of SPV-1 with other F-BAR subfamilies, SPV-1 did not generate tubules when overexpressed (**Figure 28**), as is usually the case with other F-BAR domain subfamily proteins (Heath and Insall, 2008; Tanaka-Takiguchi et al., 2013; Zaidel-Bar et al., 2010). It will be interesting to test if the F-BAR domain of SPV-1 and its human orthologs are capable of inducing the formation of tubules in either mammalian cells or liposomes as was shown for the F-BAR domain of FBP17 and CIP4 (Frost et al., 2009; Tanaka-Takiguchi et al., 2013). If indeed the F-BAR domain of the SPV-1 family is unable to tubulate membranes, it makes this noval family of F-BAR domains unique in that it solely functions to sense and bind to membrane with suitably curved surfaces. It will be interesting to identify the differences in structure or amino acid sequences that distinguish between the curvature-sensing or membrane-tubulating properties of the F-BAR domain.
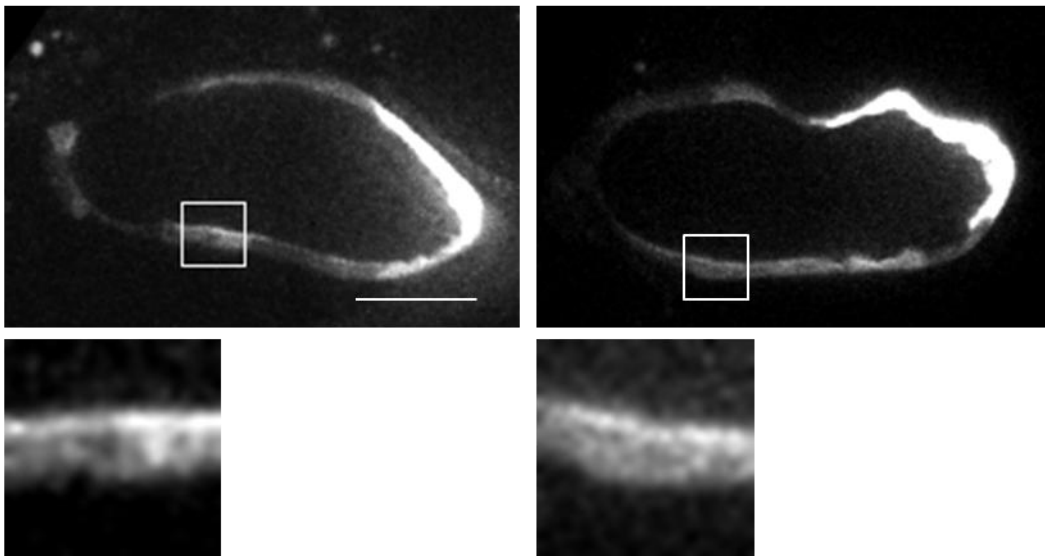
Figure 28: No observable membrane invaginations in the spermatheca of SPV-1::GFP transgenic animals.

No discernable differences between the apical membrane of SPV-1::GFP expressing in the *spv-1(ok1498)* or overexpression of SPV-1::GFP in the wild-type background. Scale bar = 20μm.

4.4. Autoinhibition of SPV-1

Our results suggest that the activity of the RhoGAP domain is autoinhibited by its F-BAR domain when SPV-1 is cytoplasmic. Although we were unable to show a direct binding between the RhoGAP and F-BAR domains, we cannot rule out that the inhibition is a result of conformational change and steric hindrance. Indeed, there have been several reports on autoinhibition of the RhoGAP domain by a BAR domain (de Kreuk et al., 2013; Galic et al., 2014; Zaidel-Bar et al., 2010). One approach to test for autoinhibition of the RhoGAP activity would be to perform a RhoGAP assay and compare the GAP activity of full length SPV-1 with only its RhoGAP domain. However, a limitation of an in vitro assay is the requirement of purified proteins. The large size of SPV-1 protein (966kDa) could prove difficult to express and purify.

4.5. Alternative hypothesis for SPV-1 mode of action

We hypothesized that the F-BAR domain of SPV-1 serves two roles: 1) to release the inhibition on the RhoGAP domain when SPV-1 is targeted to the membrane, and 2) to physically target the RhoGAP domain at the membrane for the inactivation and hydrolysis of Rho-GTP to Rho-GDP. Since active RHO-1 is localized to the plasma membrane, we hypothezise that the physical presence of the RhoGAP domain of SPV-1 at the membrane is essential for the hydrolysis of active RHO-1. However, our results showed that while loss of the F-BAR domain from SPV-1::GFP abolished its membrane-targeting ability, the truncated protein was still able to rescue the mutant phenotype. This raised two possibilities: 1) membrane-targeting ability of SPV-1 is dispensable for its function as a negative regulator of RHO-1 activity, or 2) although SPV-1 is no longer visibly enriched at the membrane, a percentage of SPV-1 is still able to exert its RhoGAP activity on RHO-1 at the membrane by relocating to the plasma membrane through passive diffusion. Our results suggest that the latter explanation is more probable due to the fact that permanently docking SPV-1 to the membrane using a PH in place of the F-BAR domain resulted in a non-contractile spermathecae, indicating that localization of the RhoGAP domain at the membrane is essential for functionality of the RhoGAP domain. To experimentally test if cytoplasmic RhoGAP domain of SPV-1 is capable of regulating RHO-1 activity, we suggest replacing the F-BAR domain with amino acid residues 231-360 of *Listeria monocytogenes* ActA. The mitochondria-targeting sequence has been reported to to bind to the outer mitochondria membrane (Bear et al., 2000) and could act to prevent SPV-1 to be in close proximity with the plasma membrane. This could directly test if cytoplasmic SPV-1 could result in RHO-1 inactivation, hence highlighting the importance of an F-BAR domain to transiently locate SPV-1 to the membrane.

4.6. Changes in membrane topology with SPV-1 translocation

We hypothesize that the release of an oocyte into the spermatheca results in the stretching of spermatheca cells, flattening of membrane folds, and detachment of SPV-1 from the membrane. On the contrary, exit of the newly fertilized embryo from the spermatheca would lead to the collapse of the spermatheca pouch, reformation of membrane folds, and recruitment of SPV-1 to the membrane. Although the convoluted membrane of the spermatheca during the resting stage has been documented using EM, the dynamic change on the membrane topology during embryo transit is currently unknown. Performing EM imaging on an embryo-filled spermatheca during would reveal the difference in membrane topology between the 'empty' and 'filled' spermatheca state. However, EM imaging is unable to capture the dynamic changes in the membrane properties during embryo transit to correspond with the gradual detachment of SPV-1 from the membrane. Furthermore, we were unable to visualize the recruitment of SPV-1 back to the membrane upon embryo exit as the collapsed spermatheca hindered viewing of the apical membrane. To indirectly show the recruitment of SPV-1 to the plasma membrane upon embryo exit, we utilized a heterologous system whereby the F-BAR domain of SPV-1 was expressed in HeLa cells. Formation of membrane convolution has been report for CHO cells upon trypsin treatment (Kapustina et al., 2013). We successfully demonstrated that F-BAR::GFP is recruited to the plasma membrane of HeLa cells upon trypsinization. However, we did not observe the reattachment and spreading of HeLa cells in the immediate timepoint post-trypsin treatment, hence we were unable to observe the detachment of the F-BAR domain from the membrane. An alternative method to directly test the curvature-sensing ability of the F-BAR domain, we propose to modify the cell area or cell volume as a means to alter membrane topology. Mouse embryonic

fibroblasts (MEFs) have been shown to modulate its cell membrane properties upon stretching or change in osmolarity (Kosmalska et al., 2015). Similar approach can be adapted for cyclical modification of the HeLa cell membrane to mimic spermathecal stretching events and to observe for the translocation of SPV-1.

4.7. Proposed mechanical regulation of RHGF-1 in the spermatheca

Previous reports have identified LARG as the human ortholog of RHGF-1 (Shaye and Greenwald, 2011; Ziel et al., 2009). Studies on human LARG described activation of RhoA downstream of LARG following mechanical stretching (Abiko et al., 2015; Guilluy et al., 2011; Lessey-Morillon et al., 2014). We hypothesize that a similar mechanism could be at play in the spermatheca, whereby oocyte entry serves as a mechanical signal to initiate RHO-1 activation through RHGF-1. LARG has been reported to be recruited to focal adhesions upon tensional force applied to the integrin receptors (Guilluy et al., 2011). Integrin receptors are heterodimers composed of alpha and beta subunits. In *C. elegans*, structures analogous to focal adhesions are termed dense bodies and have mostly been studied in the connection between muscle cells and the extracellular matrix (Lecroisey et al., 2007). *C. elegans* has two alpha integrin subunit orthologs: *ina-1* (Baum and Garriga, 1997) and *pat-2* (Williams and Waterston, 1994), and a single beta subunit ortholog: *pat-3* (Gettner et al., 1995; Williams and Waterston, 1994). The presence of *pat-3* has been observed in the spermatheca from MH25 anti-pat-3 antibody staining as a weak and diffusive pattern (Kovacevic and Cram, 2010). Using a worm strain expressing PAT-3::GFP, we identified expression in the spermatheca, which localized to the basal membrane of the spermathecal cells (Figure 29A). We have also successfully observed INA-1::GFP in the spermatheca, although the expression was more diffused (Figure 29B). Taken together, the presence of integrins in the spermatheca is consistent with the hypothesis that during embryo transit, mechanical stretching of the spermathecal cells could be transmitted through INA-1, PAT-3 and possibly PAT-2 and leads to the recruitment and activation of RHGF-1 to initiate downstream constriction events through the RHO-1/LET-502 signaling pathway. It will be interesting to knockdown *C. elegans*

integrins in the *spv-1 (ok1498)* background to determine if loss of the integrin components would reduce RHO-1 activation hence rescue the hypercontractile phenotype of the *spv-1 (ok1498)* mutant.
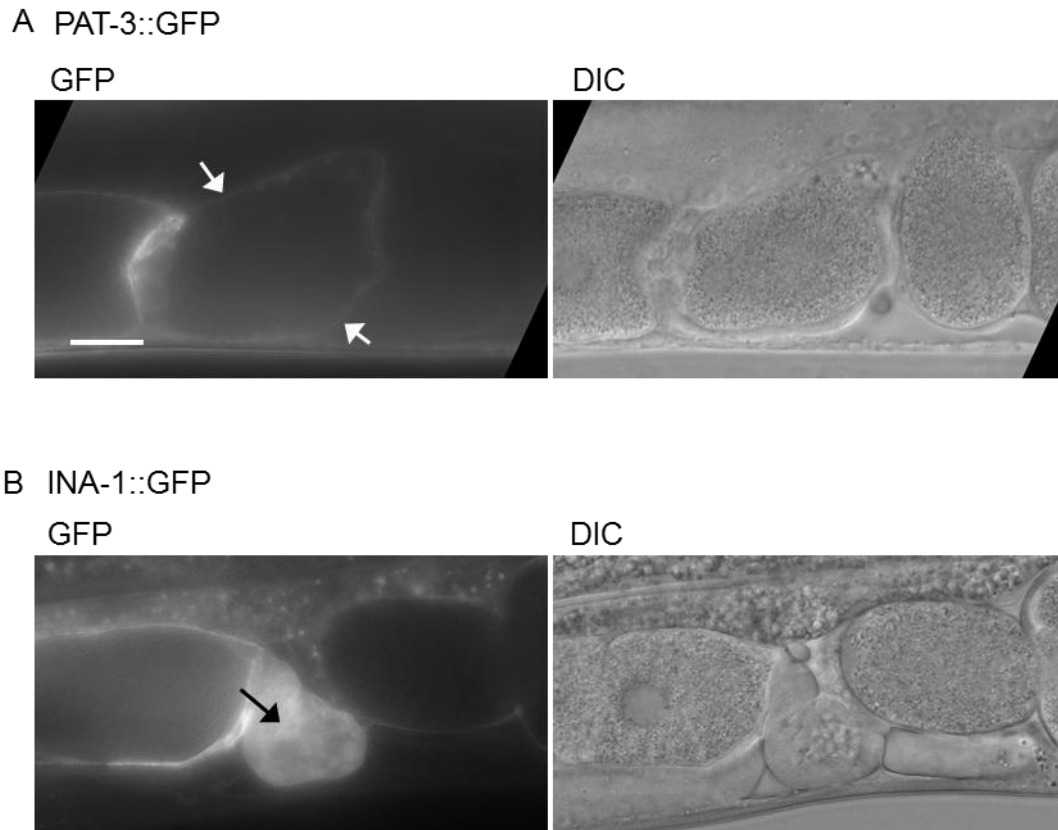
Figure 29: Expression pattern of *C. elegans* integrins in the spermatheca.

(A) PAT-3::GFP expression is enriched at the basal membrane of the spermatheca (arrows). Scale bar = 20µm.
(B) INA-1::GFP expressed in a diffused manner in the spermatheca (arrow).

4.8. Additional RhoGEFs that may function in parallel with RHGF-1 to activate RHO-1

Since the spermatheca still retained a weak contractile ability with *rhgf-1* knockdown (Figure 21), it is highly probable that *rhgf-1* is not the sole activator of RHO-1 during embryo transit. From the results of RNAi knockdown of RhoGEFs in the background of *spv-1 (ok1498)* (Table 5), both *Y105E8A.25* and *unc-73* scored 7/10 in the number of worms with embryos resembling wild-type morphology, which gave an indication that both genes could be involved in the regulation of RHO-1 activity in the spermatheca alongside *rhgf-1*. However, we were unable to reproduce the rescue of *spv-1(ok1498)* spermatheca overconstriction by *unc-73 RNAi* knockdown. Henceforth, we shall continue to characterize *Y105E8A.25*. One approach to test for redundancy is to perform a double knockdown of *rhgf-1* with *Y105E8A.25*. We should expect a severe embryo trapping phenotype resulted from a further depletion of RHO-1 if *Y105E8A.25* is indeed demonstrating RhoGEF activity in the spermatheca. Y105E8A.25 is an uncharacterized protein with no known protein domains apart from the RhoGEF domain. Generation of a reporter strain and a null mutant allele will greatly facilitate the characterization of this novel gene.

4.9. Interplay between RhoA and the calcium signaling pathway in contractile regulation of an epithelial tube.

The myoepithelial pouch that forms the *C. elegans* spermatheca is highly analogous in terms of structure and function to contractile smooth muscle tubes such as blood vessels, respiratory tract and salivary ducts in mammals. Abnormal smooth muscle contractions in these tissues result in severe pathological conditions such as asthma and hypertension. Both RhoA and calcium signaling have been shown to be essential for the constriction of airway smooth muscle cells and blood vessels (Chiba and Misawa, 2004). Although, these two pathways have long been established, they are usually identified as two independent pathways, converging at the level of myosin light chain phosphorylation. Kovacevic and colleagues reported a correlation between mechanical stretching of the spermatheca during oocyte entry and a rise in calcium levels to initiate spermathecal constriction and embryo exit (Kovacevic et al., 2013). The oocyte entry-dependent calcium release is regulated by PLC-1 and its downstream partners. They postulated that PLC-1 could be under the regulation of RHO-1, as suggested by studies conducted in mammalian cells (Wing et al., 2003). An ongoing collaboration with the Cram lab (Northeastern University, Boston, MA) is focused on characterization of the calcium activation profile in worms depleted of *spv-1* and *rhgf-1* and performing spatio-temporal correlation between RHO-1 activity and the calcium levels in the spermatheca. Preliminary findings indicate that calcium level is elevated precociously in the *spv-1 (ok1498)* mutant, indicating RHO-1 to function upstream of PLC-1-mediated calcium release. However, truncation of the RHO-1-binding site in PLC-1 did not affect calcium levels, suggesting an indirect regulation between RHO-1 and PLC-1 (Erin Cram, personal communication).

4.10.   Mechanical changes in the spermatheca during embryo transit

Although a dramatic physical change in cell shape is observed in the spermathecal during embryo transit, changes in membrane tension of the spermathecal cells have not been measured. Based on the transient membrane localization of SPV-1, we hypothesize that the loss of membrane curvature during embryo transit could correspond with increase in membrane tension. Laser microsurgery is an established method for estimating forces in and between cells to better understand tissue mechanics and morphogenesis (Rauzi and Lenne, 2011). Laser ablation experiments could serve as a tool to quantitatively compare between the mechanical forces involved during the various stages of embryo transit. An alternatively approach could be the use of a FRET-based tension sensor that incorporates a tension sensing module into the coding sequence of the *unc-70* gene which has been recently optimized for detection of mechanical tension in *C. elegans* (Kelley et al., 2015). Together, these data would give us a better understanding of the mechanical properties of the spermatheca during the embryo transit process.

4.11. Spatio-temporal regulation of RhoA activation

RhoA-mediated signaling can stimulate opposing cellular processes. For example, RhoA is required to promote junction formation and apical constriction, but is also essential for weakening of cell adhesion and preventing cell spreading (Etienne-Manneville and Hall, 2002; Terry et al., 2010). In migrating fibroblast cells, RhoA has been documented to be active simultaneously at the leading edge of protruding lamellae and also the rear during tail retraction events (Pertz et al., 2006). Hence, the activation of RhoA has to be coordinated in space and time to restrict its activity at discrete subcellular location for the regulation of specific cellular processes.

The diversity of RhoGEF and RhoGAP proteins far outnumber the RhoGTPases. This discrepancy could prove to be an evolutionary advantage for a more precise regulation over the activity of RhoGTPases. One strategy for spatial control of RhoA activation is to have the Rho regulators occupying distinct intracellular niches within the cell. At the epithelial junction, RhoA is essential for the formation and maintenance of the tight and adherens junctions mediated by the actomyosin cytoskeleton (Nusrat et al., 1995; Yamada and Nelson, 2007). p114RhoGEF is a tight junction-associated RhoGEF that regulates epithelial junction assembly through spatially-localized activation of junctional RhoA (Terry et al., 2011). During collective migration in bronchial epithelial cells, the RhoGAP protein Myosin-IXA is spatially recruited to nascent adhesion sites and temporarily limits RhoA-mediated contractile forces during the early stages of cell-cell contact formation (Omelchenko and Hall, 2012). These examples demonstrate the precise targeting of RhoA regulators for proper regulation of specific RhoA-dependent cellular functions.

In addition to spatial regulation, activation of RhoA also needs to be temporally coordinated. For example, RhoA activity is elevated by an internal signal during onset of mitosis to mediate cell rounding and stiffening of the cell cortex (Maddox and Burridge, 2003). Upon mitotic onset, phosphorylation and activation of the RhoGEF Ect2, combined with the phosphorylation and inactivation of GAP p190RhoGAP, results in a global increase in RhoA activity (Maddox and Burridge, 2003; Matthews et al., 2012). Several lines of evidence have also described the temporal regulation of RhoGEFs and RhoGAPs in response to external stimuli. Phosphorylation and activation of the RhoGEF vav2 upon cyclic stretching has been reported in mesangial cells (Peng et al., 2010) while shear stress in the endothelial cells regulate p190GAP activity in a biphasic manner (Yang et al., 2011).

Our findings on the membrane-curvature-mediated relocalization of the RhoGAP SPV-1, together with its counterpart RhoGEF RHGF-1, provide further insight on the mechanism governing spatio-temporal control of RhoA regulation in the context of cyclical regulation of a contractile tube. The regulation of RhoA activity will directly impact the activity of Rho kinase in the phosphorylation of MLC, thus affecting contractility of smooth muscle cells in an epithelial tube setting. Furthermore, evidence for mammalian cell studies have proposed RhoA to function upstream of PLC-1 and calcium release in the regulation of smooth muscle contractions. Hence, our study on the membrane curvature-dependent translocation of SPV-1 as a means to regulate RhoA activity provides a novel understanding to how the cyclical regulation of molecular players in the Rho kinase and calcium pathway are achieved.

4.12. Signaling downstream of BAR domain curvature sensing

Members of the BAR domain superfamily are capable of sensing and binding to plasma membrane of distinct curvature. Isolated N-BAR domains of nadrin 2 and amphiphysin 1 have been demonstrated to be selectively recruited to membrane folds artificially generated by nanocones (Galic et al., 2012). The BAR domain family of proteins are functionally diverse as they are coupled to a wide variety of accessory domains (Peter et al., 2004). The selective membrane binding property of the BAR domains make them suitable candidates for spatio-temporal targeting of their partner domains to membrane sites during dynamic remodeling of the plasma membrane. The migratory cell front demonstrates an oscillatory protrusion-retraction cycle. FBP17, an F-BAR domain-containing protein, is specifically recruited to membrane invaginations at the leading edge of COS-7 cells to promote actin polymerization and protrusion formation. Formation of actin protrusions results in detachment of FBP17 from the membrane, providing a reciprocal feedback regulation on the formation of the leading edge during cell migration (Tsujita et al., 2015).

A subset of BAR domain family proteins is associated with RhoGEF or RhoGAP domains (Peter et al., 2004). ArhGAP44 possesses an N-BAR and RhoGAP domain. During neuronal development, ArhGAP44 is recruited to inwardly deformed plasma membrane sections to limit filopodia formation by local inhibition of Rac activity (Galic et al., 2014). Our results provide another example of how an F-BAR domain acts a mean for sensing of mechanical changes in the membrane property and the information is translated by an intrinsic RhoGAP domain to downstream signaling modules.

Chapter 5:

Conclusion & Perspectives

5. Conclusion and Perspectives

5.1. Universal mechanism in the cyclical regulation of contractility

In this study, we have identified two novel regulators of RHO-1 activity in the *C. elegans* spermatheca. Our findings describe the reciprocal function of SPV-1 (a RhoGAP-domain protein) and RHGF-1 (a RhoGEF-domain protein) in the cyclical regulation of spermathecal constriction. We proposed that SPV-1 acts as a mechanotransducer to relay the change in spermathecal membrane curvature during oocyte entry to biochemical signals to regulate RHO-1-mediated actomyosin contractility in the spermatheca. During oocyte entry, stretching of the spermathecal cells result in the detachment of the curvature-sensitive F-BAR domain of SPV-1 from the membrane. This removes the RhoGAP inhibition on RHO-1 activity. On the flip side, our results suggest RHGF-1 as a positive regulator of RHO-1 activation to counteract SPV-1 activity. Although our study focused on the mechanical regulation of RHO-1 activity in a contractile tube, similar mechanisms could be at play in other biological systems that display a biphasic pattern of RhoA activity. The plasma membrane is common to all cells, and could act universally as a site of mechanotransduction. Hence, the direct feedback mechanism we elucidated between a physical signal of membrane curvature and the biochemical cascade leading to actomyosin contractility could be crucial in many other cellular and tissue processes involving cell deformation, ranging from cell motility to tissue morphogenesis and wound repair.

5.2. Upstream regulators of RhoA as drug targets for diseases of the epithelial tubes

Due to the diverse roles of RhoA, it is unsurprising that its misregulation is associated with the pathogenesis of a large number of human diseases. Hence, regulation of RhoA and its downstream effectors is a popular strategy for treatment (Barman et al., 2009; Gur et al., 2011; Kume, 2008; Molli et al., 2012). In pulmonary arterial hypertension, elevated levels of RhoA activation in vascular smooth muscles was found to cause arterial constriction and remodeling of the vascular walls. Therefore, one therapeutic approach is through inhibition of the RhoA pathway (Antoniu, 2012). RhoA and its effectors have also been proposed as a treatment target for elevated contractility of the bronchial smooth muscle, the pathology of asthma (Chiba et al., 2010). Identification and characterization of upstream regulators of RhoA may provide further insights of disease pathology and development of novel drug targets.

References

Abiko, H., S. Fujiwara, K. Ohashi, R. Hiatari, T. Mashiko, N. Sakamoto, M. Sato, and K. Mizuno. 2015. Rho guanine nucleotide exchange factors involved in cyclic-stretch-induced reorientation of vascular endothelial cells. *Journal of cell science*. 128:1683-1695.

Adamson, P., H.F. Paterson, and A. Hall. 1992. Intracellular localization of the P21rho proteins. *The Journal of cell biology*. 119:617-627.

Amano, M., M. Ito, K. Kimura, Y. Fukata, K. Chihara, T. Nakano, Y. Matsuura, and K. Kaibuchi. 1996. Phosphorylation and activation of myosin by Rho-associated kinase (Rho-kinase). *The Journal of biological chemistry*. 271:20246-20249.

Andrew, D.J., and A.J. Ewald. 2010. Morphogenesis of epithelial tubes: Insights into tube formation, elongation, and elaboration. *Dev Biol*. 341:34-55.

Antoniu, S.A. 2012. Targeting RhoA/ROCK pathway in pulmonary arterial hypertension. *Expert opinion on therapeutic targets*. 16:355-363.

Aznar, S., P. Fernandez-Valeron, C. Espina, and J.C. Lacal. 2004. Rho GTPases: potential candidates for anticancer therapy. *Cancer letters*. 206:181-191.

Bando, T., T. Ikeda, and H. Kagawa. 2005. The homeoproteins MAB-18 and CEH-14 insulate the dauer collagen gene col-43 from activation by the adjacent promoter of the Spermatheca gene sth-1 in Caenorhabditis elegans. *Journal of molecular biology*. 348:101-112.

Barman, S.A., S. Zhu, and R.E. White. 2009. RhoA/Rho-kinase signaling: a therapeutic target in pulmonary hypertension. *Vascular health and risk management*. 5:663-671.

Baum, P.D., and G. Garriga. 1997. Neuronal migrations and axon fasciculation are disrupted in ina-1 integrin mutants. *Neuron*. 19:51-62.

Bear, J.E., J.J. Loureiro, I. Libova, R. Fassler, J. Wehland, and F.B. Gertler. 2000. Negative regulation of fibroblast motility by Ena/VASP proteins. *Cell*. 101:717-728.

Bernards, A., and J. Settleman. 2004. GAP control: regulating the regulators of small GTPases. *Trends Cell Biol*. 14:377-385.

Berridge, M.J., and R.F. Irvine. 1989. Inositol phosphates and cell signalling. *Nature*. 341:197-205.

Biegert, A., C. Mayer, M. Remmert, J. Soding, and A.N. Lupas. 2006. The MPI Bioinformatics Toolkit for protein sequence analysis. *Nucleic acids research*. 34:W335-339.

Boratyn, G.M., A.A. Schaffer, R. Agarwala, S.F. Altschul, D.J. Lipman, and T.L. Madden. 2012. Domain enhanced lookup time accelerated BLAST. *Biology direct*. 7:12.

Bui, Y.K., and P.W. Sternberg. 2002. Caenorhabditis elegans inositol 5-phosphatase homolog negatively regulates inositol 1,4,5-triphosphate signaling in ovulation. *Mol Biol Cell*. 13:1641-1651.

Cappello, S., C.R. Bohringer, M. Bergami, K.K. Conzelmann, A. Ghanem, G.S. Tomassy, P. Arlotta, M. Mainardi, M. Allegra, M. Caleo, J. van Hengel, C. Brakebusch, and M. Gotz. 2012. A radial glia-specific role of RhoA in double cortex formation. *Neuron*. 73:911-924.

Chen, C.S., J. Tan, and J. Tien. 2004. Mechanotransduction at cell-matrix and cell-cell contacts. *Annu Rev Biomed Eng*. 6:275-302.

Chiba, Y., K. Matsusue, and M. Misawa. 2010. RhoA, a possible target for treatment of airway hyperresponsiveness in bronchial asthma. *Journal of pharmacological sciences*. 114:239-247.

Chiba, Y., and M. Misawa. 2004. The role of RhoA-mediated Ca2+ sensitization of bronchial smooth muscle contraction in airway hyperresponsiveness. *Journal of smooth muscle research = Nihon Heikatsukin Gakkai kikanshi*. 40:155-167.

Chrzanowska-Wodnicka, M., and K. Burridge. 1996. Rho-stimulated contractility drives the formation of stress fibers and focal adhesions. *The Journal of cell biology*. 133:1403-1415.

Clandinin, T.R., J.A. DeModena, and P.W. Sternberg. 1998. Inositol trisphosphate mediates a RAS-independent response to LET-23 receptor tyrosine kinase activation in C. elegans. *Cell*. 92:523-533.

de Kreuk, B.J., A. Schaefer, E.C. Anthony, S. Tol, M. Fernandez-Borja, D. Geerts, J. Pool, L. Hambach, E. Goulmy, and P.L. Hordijk. 2013. The human minor histocompatibility antigen 1 is a RhoGAP. *PLoS one*. 8:e73962.

Etienne-Manneville, S., and A. Hall. 2002. Rho GTPases in cell biology. *Nature*. 420:629-635.

Frost, A., V.M. Unger, and P. De Camilli. 2009. The BAR domain superfamily: membrane-molding macromolecules. *Cell*. 137:191-196.

Fukata, Y., M. Amano, and K. Kaibuchi. 2001. Rho-Rho-kinase pathway in smooth muscle contraction and cytoskeletal reorganization of non-muscle cells. *Trends Pharmacol Sci*. 22:32-39.

Galic, M., S. Jeong, F.C. Tsai, L.M. Joubert, Y.I. Wu, K.M. Hahn, Y. Cui, and T. Meyer. 2012. External push and internal pull forces recruit curvature-sensing N-BAR domain proteins to the plasma membrane. *Nat Cell Biol*. 14:874-881.

Galic, M., F.C. Tsai, S.R. Collins, M. Matis, S. Bandara, and T. Meyer. 2014. Dynamic recruitment of the curvature-sensitive protein ArhGAP44 to nanoscale membrane deformations limits exploratory filopodia initiation in neurons. *eLife*. 3:e03116.

Garcia-Mata, R., E. Boulter, and K. Burridge. 2011. The 'invisible hand': regulation of RHO GTPases by RHOGDIs. *Nat Rev Mol Cell Biol*. 12:493-504.

Geiger, B., J.P. Spatz, and A.D. Bershadsky. 2009. Environmental sensing through focal adhesions. *Nat Rev Mol Cell Biol*. 10:21-33.

Gettner, S.N., C. Kenyon, and L.F. Reichardt. 1995. Characterization of beta pat-3 heterodimers, a family of essential integrin receptors in C. elegans. *The Journal of cell biology*. 129:1127-1141.

Grinnell, F., C.H. Ho, E. Tamariz, D.J. Lee, and G. Skuta. 2003. Dendritic fibroblasts in three-dimensional collagen matrices. *Mol Biol Cell*. 14:384-395.

Guilluy, C., V. Swaminathan, R. Garcia-Mata, E.T. O'Brien, R. Superfine, and K. Burridge. 2011. The Rho GEFs LARG and GEF-H1 regulate the mechanical response to force on integrins. *Nat Cell Biol*. 13:722-727.

Gur, S., P.J. Kadowitz, and W.J. Hellstrom. 2011. RhoA/Rho-kinase as a therapeutic target for the male urogenital tract. *The journal of sexual medicine*. 8:675-687.

Heath, R.J., and R.H. Insall. 2008. F-BAR domains: multifunctional regulators of membrane curvature. *Journal of cell science*. 121:1951-1954.

Hiley, E., R. McMullan, and S.J. Nurrish. 2006. The Galpha12-RGS RhoGEF-RhoA signalling pathway regulates neurotransmitter release in C. elegans. *The EMBO journal*. 25:5884-5895.

Huson, D.H., and C. Scornavacca. 2012. Dendroscope 3: an interactive tool for rooted phylogenetic trees and networks. *Systematic biology*. 61:1061-1067.

Itoh, T., K.S. Erdmann, A. Roux, B. Habermann, H. Werner, and P. De Camilli. 2005. Dynamin and the actin cytoskeleton cooperatively regulate plasma membrane invagination by BAR and F-BAR proteins. *Developmental cell*. 9:791-804.

Jackson, B., K. Peyrollier, E. Pedersen, A. Basse, R. Karlsson, Z. Wang, T. Lefever, A.M. Ochsenbein, G. Schmidt, K. Aktories, A. Stanley, F. Quondamatteo, M. Ladwein, K. Rottner, J. van Hengel, and C. Brakebusch. 2011. RhoA is dispensable for skin development, but crucial for contraction and directed migration of keratinocytes. *Mol Biol Cell*. 22:593-605.

Jaffe, A.B., and A. Hall. 2005. Rho GTPases: biochemistry and biology. *Annual review of cell and developmental biology*. 21:247-269.

Kapustina, M., T.C. Elston, and K. Jacobson. 2013. Compression and dilation of the membrane-cortex layer generates rapid changes in cell shape. *The Journal of cell biology*. 200:95-108.

Kariya, K., Y.K. Bui, X. Gao, P.W. Sternberg, and T. Kataoka. 2004. Phospholipase Cepsilon regulates ovulation in Caenorhabditis elegans. *Dev Biol*. 274:201-210.

Katsumi, A., J. Milanini, W.B. Kiosses, M.A. del Pozo, R. Kaunas, S. Chien, K.M. Hahn, and M.A. Schwartz. 2002. Effects of cell tension on the small GTPase Rac. *The Journal of cell biology*. 158:153-164.

Kelley, L.A., and M.J. Sternberg. 2009. Protein structure prediction on the Web: a case study using the Phyre server. *Nature protocols*. 4:363-371.

Kelley, M., J. Yochem, M. Krieg, A. Calixto, M.G. Heiman, A. Kuzmanov, V. Meli, M. Chalfie, M.B. Goodman, S. Shaham, A. Frand, and D.S. Fay. 2015. FBN-1, a fibrillin-related protein, is required for resistance of the epidermis to mechanical deformation during C. elegans embryogenesis. *eLife*. 4.

Kimura, K., M. Ito, M. Amano, K. Chihara, Y. Fukata, M. Nakafuku, B. Yamamori, J. Feng, T. Nakano, K. Okawa, A. Iwamatsu, and K. Kaibuchi. 1996. Regulation of myosin phosphatase by Rho and Rho-associated kinase (Rho-kinase). *Science*. 273:245-248.

Kishore, R.S., and M.V. Sundaram. 2002. ced-10 Rac and mig-2 function redundantly and act with unc-73 trio to control the orientation of vulval cell divisions and migrations in Caenorhabditis elegans. *Dev Biol*. 241:339-348.

Kosmalska, A.J., L. Casares, A. Elosegui-Artola, J.J. Thottacherry, R. Moreno-Vicente, V. Gonzalez-Tarrago, M.A. del Pozo, S. Mayor, M. Arroyo, D. Navajas, X. Trepat, N.C. Gauthier, and P. Roca-Cusachs. 2015. Physical principles of membrane remodelling during cell mechanoadaptation. *Nature communications*. 6:7292.

Kovacevic, I., and E.J. Cram. 2010. FLN-1/filamin is required for maintenance of actin and exit of fertilized oocytes from the spermatheca in C. elegans. *Dev Biol*. 347:247-257.

Kovacevic, I., and E.J. Cram. 2013. Filamin and Phospholipase C-epsilon are required for calcium signaling in the Caenorhabditis elegans Spermatheca. *Worm*. 2:e25717.

Kovacevic, I., J.M. Orozco, and E.J. Cram. 2013. Filamin and phospholipase C-epsilon are required for calcium signaling in the Caenorhabditis elegans spermatheca. *PLoS genetics*. 9:e1003510.

Kume, H. 2008. RhoA/Rho-kinase as a therapeutic target in asthma. *Current medicinal chemistry*. 15:2876-2885.

Lang, P., F. Gesbert, J.M. Thiberge, F. Troalen, H. Dutartre, P. Chavrier, and J. Bertoglio. 1993. Characterization of a monoclonal antibody specific for the

Ras-related GTP-binding protein Rho A. *Biochem Biophys Res Commun*. 196:1522-1528.

Lecroisey, C., L. Segalat, and K. Gieseler. 2007. The C. elegans dense body: anchoring and signaling structure of the muscle. *Journal of muscle research and cell motility*. 28:79-87.

Lessey, E.C., C. Guilluy, and K. Burridge. 2012. From mechanical force to RhoA activation. *Biochemistry*. 51:7420-7432.

Lessey-Morillon, E.C., L.D. Osborne, E. Monaghan-Benson, C. Guilluy, E.T. O'Brien, R. Superfine, and K. Burridge. 2014. The RhoA guanine nucleotide exchange factor, LARG, mediates ICAM-1-dependent mechanotransduction in endothelial cells to stimulate transendothelial migration. *Journal of immunology*. 192:3390-3398.

Lints, R., and D.H. Hall. 2005. Reproductive system, part II. *WormAtlas*.

Loirand, G., and P. Pacaud. 2010. The role of Rho protein signaling in hypertension. *Nature reviews. Cardiology*. 7:637-647.

Maddox, A.S., and K. Burridge. 2003. RhoA is required for cortical retraction and rigidity during mitotic cell rounding. *The Journal of cell biology*. 160:255-265.

Marchler-Bauer, A., S. Lu, J.B. Anderson, F. Chitsaz, M.K. Derbyshire, C. DeWeese-Scott, J.H. Fong, L.Y. Geer, R.C. Geer, N.R. Gonzales, M. Gwadz, D.I. Hurwitz, J.D. Jackson, Z. Ke, C.J. Lanczycki, F. Lu, G.H. Marchler, M. Mullokandov, M.V. Omelchenko, C.L. Robertson, J.S. Song, N. Thanki, R.A. Yamashita, D. Zhang, N. Zhang, C. Zheng, and S.H. Bryant. 2011. CDD: a Conserved Domain Database for the functional annotation of proteins. *Nucleic acids research*. 39:D225-229.

Matthews, H.K., U. Delabre, J.L. Rohn, J. Guck, P. Kunda, and B. Baum. 2012. Changes in Ect2 localization couple actomyosin-dependent cell shape changes to mitotic progression. *Developmental cell*. 23:371-383.

McCarter, J., B. Bartlett, T. Dang, and T. Schedl. 1999. On the control of oocyte meiotic maturation and ovulation in Caenorhabditis elegans. *Dev Biol*. 205:111-128.

McDonnell, A.V., T. Jiang, A.E. Keating, and B. Berger. 2006. Paircoil2: improved prediction of coiled coils from sequence. *Bioinformatics*. 22:356-358.

McMahon, H.T., and J.L. Gallop. 2005. Membrane curvature and mechanisms of dynamic cell membrane remodelling. *Nature*. 438:590-596.

Miller, M.A., V.Q. Nguyen, M.H. Lee, M. Kosinski, T. Schedl, R.M. Caprioli, and D. Greenstein. 2001. A sperm cytoskeletal protein that signals oocyte meiotic maturation and ovulation. *Science*. 291:2144-2147.

Mim, C., and V.M. Unger. 2012. Membrane curvature and its generation by BAR proteins. *Trends in biochemical sciences*. 37:526-533.

Minc, N., D. Burgess, and F. Chang. 2011. Influence of cell geometry on division-plane positioning. *Cell*. 144:414-426.

Molli, P.R., M.B. Pradhan, S.H. Advani, and N.R. Naik. 2012. RhoA: a therapeutic target for chronic myeloid leukemia. *Molecular cancer*. 11:16.

Nelson, C.M., D.M. Pirone, J.L. Tan, and C.S. Chen. 2004. Vascular endothelial-cadherin regulates cytoskeletal tension, cell spreading, and focal adhesions by stimulating RhoA. *Mol Biol Cell*. 15:2943-2953.

Nghe, P., S. Boulineau, S. Gude, P. Recouvreux, J.S. van Zon, and S.J. Tans. 2013. Microfabricated polyacrylamide devices for the controlled culture of growing cells and developing organisms. *PloS one*. 8:e75537.

Notredame, C., D.G. Higgins, and J. Heringa. 2000. T-Coffee: A novel method for fast and accurate multiple sequence alignment. *Journal of molecular biology*. 302:205-217.

Nusrat, A., M. Giry, J.R. Turner, S.P. Colgan, C.A. Parkos, D. Carnes, E. Lemichez, P. Boquet, and J.L. Madara. 1995. Rho protein regulates tight junctions and perijunctional actin organization in polarized epithelia. *Proceedings of the National Academy of Sciences of the United States of America*. 92:10629-10633.

Omelchenko, T., and A. Hall. 2012. Myosin-IXA regulates collective epithelial cell migration by targeting RhoGAP activity to cell-cell junctions. *Current biology : CB*. 22:278-288.

Pathak, M.M., J.L. Nourse, T. Tran, J. Hwe, J. Arulmoli, D.T. Le, E. Bernardis, L.A. Flanagan, and F. Tombola. 2014. Stretch-activated ion channel Piezo1 directs lineage choice in human neural stem cells. *Proceedings of the National Academy of Sciences of the United States of America*. 111:16148-16153.

Peng, F., B. Zhang, A.J. Ingram, B. Gao, Y. Zhang, and J.C. Krepinsky. 2010. Mechanical stretch-induced RhoA activation is mediated by the RhoGEF Vav2 in mesangial cells. *Cellular signalling*. 22:34-40.

Pertz, O., L. Hodgson, R.L. Klemke, and K.M. Hahn. 2006. Spatiotemporal dynamics of RhoA activity in migrating cells. *Nature*. 440:1069-1072.

Peter, B.J., H.M. Kent, I.G. Mills, Y. Vallis, P.J. Butler, P.R. Evans, and H.T. McMahon. 2004. BAR domains as sensors of membrane curvature: the amphiphysin BAR structure. *Science*. 303:495-499.

Qualmann, B., D. Koch, and M.M. Kessels. 2011. Let's go bananas: revisiting the endocytic BAR code. *The EMBO journal*. 30:3501-3515.

Rao, Y., Q. Ma, A. Vahedi-Faridi, A. Sundborger, A. Pechstein, D. Puchkov, L. Luo, O. Shupliakov, W. Saenger, and V. Haucke. 2010. Molecular basis for SH3 domain regulation of F-BAR-mediated membrane deformation. *Proceedings of the National Academy of Sciences of the United States of America*. 107:8213-8218.

Rauzi, M., and P.F. Lenne. 2011. Cortical forces in cell shape changes and tissue morphogenesis. *Current topics in developmental biology*. 95:93-144.

Rodger, I.W. 1992. Asthma. Airway smooth muscle. *British medical bulletin*. 48:97-107.

Rossman, K.L., C.J. Der, and J. Sondek. 2005. GEF means go: turning on RHO GTPases with guanine nucleotide-exchange factors. *Nat Rev Mol Cell Biol*. 6:167-180.

Roy, A., A. Kucukural, and Y. Zhang. 2010. I-TASSER: a unified platform for automated protein structure and function prediction. *Nature protocols*. 5:725-738.

Saras, J., P. Franzen, P. Aspenstrom, U. Hellman, L.J. Gonez, and C.H. Heldin. 1997. A novel GTPase-activating protein for Rho interacts with a PDZ domain of the protein-tyrosine phosphatase PTPL1. *The Journal of biological chemistry*. 272:24333-24338.

Shaye, D.D., and I. Greenwald. 2011. OrthoList: a compendium of C. elegans genes with human orthologs. *PloS one*. 6:e20085.

Spencer, A.G., S. Orita, C.J. Malone, and M. Han. 2001. A RHO GTPase-mediated pathway is required during P cell migration in Caenorhabditis elegans. *Proceedings of the National Academy of Sciences of the United States of America*. 98:13132-13137.

Tan, P.Y., and R. Zaidel-Bar. 2015. Transient membrane localization of SPV-1 drives cyclical actomyosin contractions in the C. elegans spermatheca. *Current biology : CB*. 25:141-151.

Tanaka-Takiguchi, Y., T. Itoh, K. Tsujita, S. Yamada, M. Yanagisawa, K. Fujiwara, A. Yamamoto, M. Ichikawa, and K. Takiguchi. 2013. Physicochemical analysis from real-time imaging of liposome tubulation reveals the characteristics of individual F-BAR domain proteins. *Langmuir : the ACS journal of surfaces and colloids*. 29:328-336.

Terry, S., M. Nie, K. Matter, and M.S. Balda. 2010. Rho signaling and tight junction functions. *Physiology (Bethesda)*. 25:16-26.

Terry, S.J., C. Zihni, A. Elbediwy, E. Vitiello, I.V. Leefa Chong San, M.S. Balda, and K. Matter. 2011. Spatially restricted activation of RhoA signalling at epithelial junctions by p114RhoGEF drives junction formation and morphogenesis. *Nat Cell Biol*. 13:159-166.

Thomson, D.A.W. 1992. On Growth and Form. Dover Publications. 1116.

Tse, Y.C., M. Werner, K.M. Longhini, J.C. Labbe, B. Goldstein, and M. Glotzer. 2012. RhoA activation during polarization and cytokinesis of the early Caenorhabditis elegans embryo is differentially dependent on NOP-1 and CYK-4. *Mol Biol Cell*. 23:4020-4031.

Tsujita, K., S. Suetsugu, N. Sasaki, M. Furutani, T. Oikawa, and T. Takenawa. 2006. Coordination between the actin cytoskeleton and membrane deformation by a novel membrane tubulation domain of PCH proteins is involved in endocytosis. *The Journal of cell biology*. 172:269-279.

Tsujita, K., T. Takenawa, and T. Itoh. 2015. Feedback regulation between plasma membrane tension and membrane-bending proteins organizes cell polarity during leading edge formation. *Nat Cell Biol*. 17:749-758.

Van Eyk, J.E., D.K. Arrell, D.B. Foster, J.D. Strauss, T.Y. Heinonen, E. Furmaniak-Kazmierczak, G.P. Cote, and A.S. Mak. 1998. Different molecular mechanisms for Rho family GTPase-dependent, Ca2+-independent contraction of smooth muscle. *The Journal of biological chemistry*. 273:23433-23439.

Vogel, V., and M. Sheetz. 2006. Local force and geometry sensing regulate cell functions. *Nat Rev Mol Cell Biol*. 7:265-275.

von Wichert, G., G. Jiang, A. Kostic, K. De Vos, J. Sap, and M.P. Sheetz. 2003. RPTP-alpha acts as a transducer of mechanical force on alphav/beta3-integrin-cytoskeleton linkages. *The Journal of cell biology*. 161:143-153.

Watanabe, N., T. Kato, A. Fujita, T. Ishizaki, and S. Narumiya. 1999. Cooperation between mDia1 and ROCK in Rho-induced actin reorganization. *Nat Cell Biol*. 1:136-143.

Waterhouse, A.M., J.B. Procter, D.M. Martin, M. Clamp, and G.J. Barton. 2009. Jalview Version 2--a multiple sequence alignment editor and analysis workbench. *Bioinformatics*. 25:1189-1191.

Williams, B.D., and R.H. Waterston. 1994. Genes critical for muscle development and function in Caenorhabditis elegans identified through lethal mutations. *The Journal of cell biology*. 124:475-490.

Wing, M.R., J.T. Snyder, J. Sondek, and T.K. Harden. 2003. Direct activation of phospholipase C-epsilon by Rho. *The Journal of biological chemistry*. 278:41253-41258.

Wissmann, A., J. Ingles, and P.E. Mains. 1999. The Caenorhabditis elegans mel-11 myosin phosphatase regulatory subunit affects tissue contraction in the

somatic gonad and the embryonic epidermis and genetically interacts with the Rac signaling pathway. *Dev Biol*. 209:111-127.

Wu, Y.C., T.W. Cheng, M.C. Lee, and N.Y. Weng. 2002. Distinct rac activation pathways control Caenorhabditis elegans cell migration and axon outgrowth. *Dev Biol*. 250:145-155.

Yamada, S., and W.J. Nelson. 2007. Localized zones of Rho and Rac activities drive initiation and expansion of epithelial cell-cell adhesion. *The Journal of cell biology*. 178:517-527.

Yang, B., C. Radel, D. Hughes, S. Kelemen, and V. Rizzo. 2011. p190 RhoGTPase-activating protein links the β1 integrin/caveolin-1 mechanosignaling complex to RhoA and actin remodeling. *Arterioscler Thromb Vasc Biol*. 31:376-383.

Zaidel-Bar, R., M.J. Joyce, A.M. Lynch, K. Witte, A. Audhya, and J. Hardin. 2010. The F-BAR domain of SRGP-1 facilitates cell-cell adhesion during C. elegans morphogenesis. *The Journal of cell biology*. 191:761-769.

Zaidel-Bar, R., G. Zhenhuan, and C. Luxenburg. 2015. The contractome - a systems view of actomyosin contractility in non-muscle cells. *Journal of cell science*. 128:2209-2217.

Zhao, H., A. Pykalainen, and P. Lappalainen. 2011. I-BAR domain proteins: linking actin and plasma membrane dynamics. *Current opinion in cell biology*. 23:14-21.

Ziel, J.W., D.Q. Matus, and D.R. Sherwood. 2009. An expression screen for RhoGEF genes involved in C. elegans gonadogenesis. *Gene expression patterns : GEP*. 9:397-403.